



Investigating plasma motion of magnetic clouds at 1 AU through a velocity-modified cylindrical force-free flux rope model

Yuming Wang,^{1,2,*} Zhenjun Zhou,¹ Chenglong Shen,^{1,2} Rui Liu,^{1,3} and S. Wang¹

¹CAS Key Laboratory of Geospace Environment, Department of Geophysics and Planetary Sciences, University of Science and Technology of China, Hefei, Anhui 230026, China

²Synergetic Innovation Center of Quantum Information and Quantum Physics, University of Science and Technology of China, Hefei, Anhui 230026, China

³Mengcheng National Geophysical Observatory, School of Earth and Space Sciences, University of Science and Technology of China, Hefei, China

* Corresponding Author, Contact: ymwang@ustc.edu.cn

Contents

1	Introduction	1
2	Model and Events	2
2.1	Velocity-modified cylindrical force-free flux rope model	2
2.1.1	Model description	2
2.1.2	Parameters	3
2.1.3	Evaluation of the goodness-of-fit	4
2.2	Events and model testing	5
3	Effects of velocity on the fitting results	7
4	Statistical properties of plasma motion	11
4.1	Linear propagating motion	11
4.2	Expanding motion	11
4.3	Poloidal motion	13
5	conclusions and discussion	14
A	Derivation of poloidal speed v_φ	16
B	Additional tables	17

that the expansion speed is correlated with the radial propagation speed and most MCs did not expand self-similarly at 1 AU. In our statistics, about 62%/17% of MCs underwent a under/over-expansion at 1 AU and the expansion rate is about 0.6 on average. Third, most interestingly, we find that a significant poloidal motion did exist in some MCs. Three speculations about the cause of the poloidal motion are therefore proposed. These findings advance our understanding of the MC's properties at 1 AU as well as the dynamic evolution of CMEs from the Sun to interplanetary space.

1 Introduction

Since first identified by *Burlaga et al.* in 1981, magnetic clouds (MCs) have been studied extensively in the past decades. They are large-scale organized magnetic structures in interplanetary space, developed from coronal mass ejections (CMEs), and play an important role in understanding the evolution of CMEs from the Sun to the heliosphere and the associated geoeffectiveness.

The current knowledge of MCs are mostly from in-situ one-dimensional observations, and various MC fitting models have been developed to reconstruct the global picture of MCs in two or three dimensions. It is now believed that an MC is a loop-like magnetic flux rope with two ends rooting on the Sun [e.g., *Burlaga et al.*, 1981; *Larson et al.*, 1997; *Janvier et al.*, 2013]. The modeling efforts mainly focus on two aspects. One is to reconstruct a realistic geometry and magnetic field configuration. In past decades, MC fitting models have been developed from cylindrically symmetrical force-free flux ropes [e.g., *Goldstein*, 1983; *Marubashi*, 1986; *Burlaga*, 1988; *Lepping et al.*, 1990; *Kumar and Rust*, 1996] gradually to asymmetrically cylindrical (non-)force-free flux ropes [e.g., *Mulligan and Russell*, 2001; *Hu and Sonnerup*, 2002; *Hidalgo et al.*, 2002a,b; *Cid et al.*, 2002; *Vandas and Romashets*, 2003] and torus-shaped flux ropes [e.g., *Romashets and Vandas*, 2003; *Marubashi and Lepping*, 2007; *Hidalgo and Nieves-Chinchilla*, 2012]. Some comparisons among various MC fitting models could be found

Abstract. Magnetic clouds (MCs) are the interplanetary counterparts of coronal mass ejections (CMEs), and usually modeled by a flux rope. By assuming the quasi-steady evolution and self-similar expansion, we introduce three types of global motion into a cylindrical force-free flux rope model, and developed a new velocity-modified model for MCs. The three types of the global motion are the linear propagating motion away from the Sun, the expanding and the poloidal motion with respect to the axis of the MC. The model is applied to 72 MCs observed by Wind spacecraft to investigate the properties of the plasma motion of MCs. First, we find that some MCs had a significant propagation velocity perpendicular to the radial direction, suggesting the direct evidence of the CME's deflected propagation and/or rotation in interplanetary space. Second, we confirm the previous results

arXiv:1502.05112v2 [astro-ph.SR] 28 Feb 2015

in the papers by, e.g., *Riley et al.* [2004], *Al-Haddad et al.* [2011] and *Al-Haddad et al.* [2013].

The other important aspect is to understand the expansion and distortion of the cross-section of a MC [e.g., *Farrugia et al.*, 1993, 1995; *Marubashi*, 1997; *Shimazu and Vandas*, 2002; *Berdichevsky et al.*, 2003; *Hidalgo*, 2003; *Owens et al.*, 2006; *Dasso et al.*, 2007; *Démoulin and Dasso*, 2009a,b; *Démoulin et al.*, 2013]. This is generally an issue about how the velocity is distributed in an MC. There are lots of observational evidence that MCs expand when propagating away from the Sun [e.g., *Klein and Burlaga*, 1982; *Berdichevsky et al.*, 2003; *Wang et al.*, 2005; *Jian et al.*, 2006; *Gulisano et al.*, 2010]. When the expansion is anisotropic, the initially circular cross-section of a MC will deform into a non-circular shape. The kinematic treatments and MHD simulations suggested that MCs may develop into an ellipse or ‘pancake’ shape [Riley et al., 2003; Riley and Crooker, 2004; Owens et al., 2006]. After exploring the parameter space of flux rope models, *Démoulin et al.* [2013] concluded that the aspect ratio of the ellipse is around 2, but not too large. On the other hand, the fitting results applying an ellipse model to the observed MCs suggested that the cross-section of MCs may be not far from a circle [See Table 1 of *Hidalgo*, 2003]. A similar result could be seen in the papers by *Hu and Sonnerup* [2001] and *Hu and Sonnerup* [2002], who used the Grad-Shafranov (GS) technique to reconstruct MCs in a 2-dimensional plane. This technique does not constrain the shape of the MC’s cross-section, but we still can find a nearly circular cross-section, particularly for the inner core. Thus, it may be acceptable to assume a circular cross-section of an MC at 1 AU.

Furthermore, expansion is only one type of the motion of the MC plasma. Imagining a segment of an MC, which is approximately a cylindrical flux rope (refer to Fig.1b), one may assume that there are at least three types of the global plasma motion: linear propagating motion, $\mathbf{v}_c = (v_x, v_y, v_z)$, expanding motion, v_e and poloidal motion, v_p . \mathbf{v}_c is the velocity in a rest reference frame, e.g., GSE coordinate system (X, Y, Z) , in which spacecraft movement could be ignored during the passage of an MC. v_e and v_p are both the speeds in a plane perpendicular to the MC’s axis. By applying a cylindrical coordinate system, (r, φ, z) , sticking to the axis of the MC, we have $v_e = v_r$ and $v_p = v_\varphi$.

Most of previous studies of fitting locally observed MCs simply assumed that MCs propagate radially from the Sun, which means that $\mathbf{v}_c \approx v_x \hat{\mathbf{X}}$. However, statistical and case studies of the propagation and geoeffectiveness of CMEs suggested CME may experience a deflected propagation in interplanetary space [Wang et al., 2002, 2004, 2006a, 2014; *Kilpua et al.*, 2009; *Rodriguez et al.*, 2011; *Lugaz*, 2010; *Isavnin et al.*, 2013, 2014]. It will obviously provide a non-radial component of the linear propagation motion. Besides, the orientation of the MC axis may probably rotate when an MC propagates in interplanetary space [e.g., *Rust et al.*, 2005; *Wang et al.*, 2006b; *Yurchyshyn*, 2008; *Yurchyshyn et al.*, 2009; *Vourlidis et al.*, 2011; *Nieves-Chinchilla et al.*, 2012; *Isavnin et al.*, 2014]. It is another source of the non-radial motion. The pictures of both deflection and rotation are mainly established on indirect evidence and models. Thus it is interesting to seek any signatures of non-radial motion from in-situ data.

As to the poloidal motion of plasma in MCs, there is so far no particular study. But some phenomena hint at the possible existence of such a motion. One of them is the strong field-aligned streams of suprathermal electrons in MCs [e.g., *Larson et al.*, 1997]. Another is the frequently observed plasma flows in prominences and coronal loops in the solar corona. Prominences and coronal loops may be a part of a MC if they are involved in an eruption. If plasma poloidal motion did exist in MCs, we will shed new light on the dynamic evolution of CMEs.

The aim of the present work is to investigate the plasma motion of MCs from in-situ data with the aid of a flux rope model. As the first attempt, we utilize a relatively simple and ideal flux rope model, which is cylindrically symmetrical and force-free, but with all the three components of the plasma motion taken into account. One could go to the web page http://space.ustc.edu.cn/dreams/mc_fitting/ to run our model. The details of the model and method we employed in this work are described in the next section.

2 Model and Events

2.1 Velocity-modified cylindrical force-free flux rope model

2.1.1 Model description

Our model is developed from the cylindrically symmetrical force-free flux rope model that has been widely used in many previous studies [e.g., *Lepping et al.*, 1990]. The following coordinate systems are used. One is the GSE coordinate system, (X, Y, Z) , in which $\hat{\mathbf{X}}$ is along the Sun-Earth (or Sun-spacecraft) line pointing toward the Sun, $\hat{\mathbf{Z}}$ is a northward vector perpendicular to the ecliptic plane and $\hat{\mathbf{Y}}$ completes the right-handed coordinate system. Another is a cylindrical coordinate system in the MC frame, (r, φ, z) , with $\hat{\mathbf{z}}$ along the axis of the flux rope, as illustrated by Figure 1a. Sometimes to show the pattern of magnetic field and velocity, one more Cartesian coordinates in the MC frame, (x', y', z') , is used, in which $\hat{\mathbf{z}}'$ is identical with $\hat{\mathbf{z}}$, $\hat{\mathbf{x}}'$ -axis is the projection of the observational path on the plane perpendicular to $\hat{\mathbf{z}}'$, approximately directed toward the Earth and $\hat{\mathbf{y}}'$ completes the right-hand coordinate system (see Fig.12e and 13e).

The magnetic field of a cylindrical flux rope is described by *Lundquist* [1950] solution in the coordinates (r, φ, z)

$$\mathbf{B}_r = 0 \quad (1)$$

$$\mathbf{B}_\varphi = HB_0 J_1(\alpha r) \hat{\boldsymbol{\varphi}} \quad (2)$$

$$\mathbf{B}_z = B_0 J_0(\alpha r) \hat{\mathbf{z}} \quad (3)$$

in which $H = \pm 1$ is the handedness or sign of the helicity, B_0 is the magnetic field strength at the axis, α is the constant force-free factor, and J_0 and J_1 are the Bessel functions of order 0 and 1, respectively. Like common treatment, we set the boundary of a flux rope at the first zero point of J_0 , which leads to $\alpha = 2.41/R$ and R is therefore the radius of the flux rope.

If any kinematic evolution of the flux rope could be ignored, the magnetic field profile along an observational path is determined once the following six parameters are known: (1) the orientation of the flux rope’s axis, i.e., the $\hat{\mathbf{z}}$ -axis, which is given by the elevation and azimuthal angles, θ and

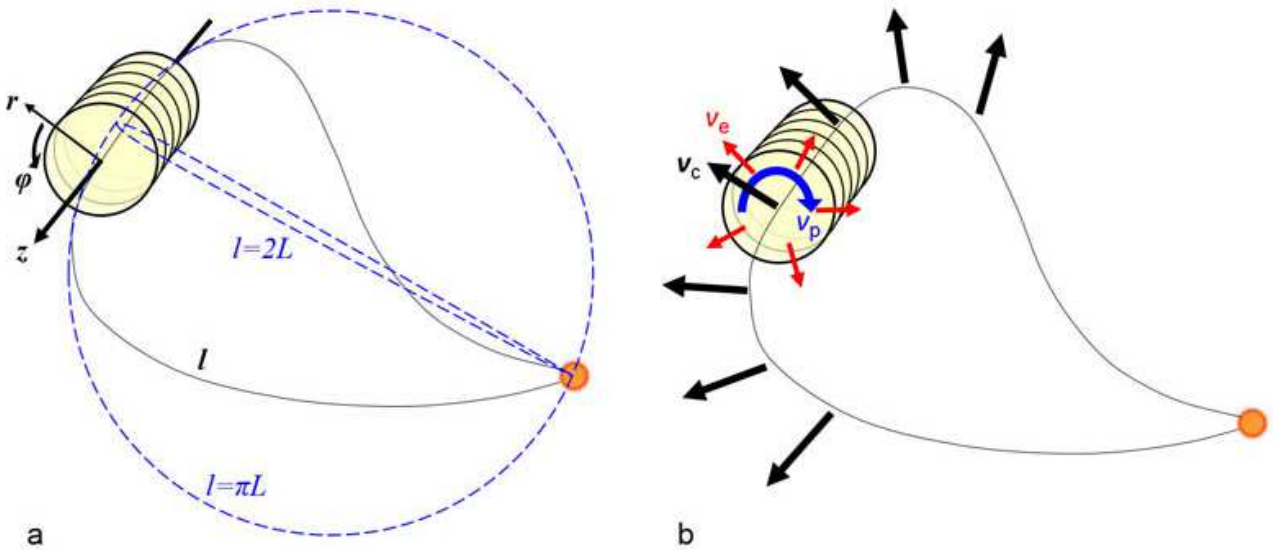


Figure 1: (a) Schematic picture of an MC at the heliocentric distance of L (adapted from Wang *et al.* [2009]). The black line indicates the looped axis of the MC with a length of l . The blue dashed lines suggest the upper and lower limits of l . (b) Illustration of the three types of global motions of an MC. The black, red and blue arrows denote the linear propagating motion, expanding motion and poloidal motion, respectively.

ϕ , in GSE coordinate system; $\theta = 0$ is in the ecliptic plane and $\theta = 0$ and $\phi = 0$ is toward the Sun, (2) the closest approach (CA) of the observational path to the flux rope's axis, given by d in units of R ; a positive/negative value of d means that the observational path is above/below the axis in (x', y', z') coordinates, i.e., $y' > 0/y' < 0$ as shown by the examples of the positive d in Fig.12e and 13e, and (3) the free parameters in Eq.1-3, which are H , B_0 and R .

After the possible plasma motion is taken into account, five additional parameters should be considered, which are $\mathbf{v}_c = (v_x, v_y, v_z)$, v_e and v_p . Here we assume that the flux rope propagates and expands uniformly and experiences a quasi-steady, self-similar expansion (or contraction) during the period of interest. Thus, \mathbf{v}_c is a constant vector, describing a global linear motion, that does not change the internal magnetic field of the flux rope.

The parameter v_e is a constant expansion speed of the boundary of the cross-section of the flux rope. The self-similar assumption gives the expansion speed at any radial distance, r , away from the flux rope's axis as

$$v_r(x) = xv_e \quad (4)$$

in which x is the normalized radial distance, equal to r/R . As a consequence, the radius of the cross-section of the flux rope evolves as follows

$$R(t) = R(t_0) + v_e(t - t_0) \quad (5)$$

in which t_0 is the initial time (or the time the observer first encountering the MC flux rope), and the magnetic field as

$$B_0(t) = B_0(t_0) \left[\frac{R(t_0)}{R(t)} \right]^2 \quad (6)$$

Eq.6 follows the magnetic flux conservation.

It should be noted that, due to the curvature of the whole looped flux rope, the propagation velocity of the different

segment of the flux rope is along the different direction as illustrated in Figure 1b, which may actually cause the expansion along the axis of the flux rope. That is also why the length of the flux rope increases as indicated by Eq.14 below. The axial expansion rate could be on the same order of the expansion rate of the flux rope's cross-section [e.g., Dasso *et al.*, 2007; Démoulin *et al.*, 2008; Nakwacki *et al.*, 2011], which guarantee a roughly self-consistent evolution of a force-free flux rope [Shimazu and Vandas, 2002].

Under the assumption of self-similar expansion and the conservations in both mass and angular momentum, the poloidal speed in the flux rope can be derived (see Appendix A) as

$$v_\phi(t, x) = k_1 f_p(x) R(t)^{-1} \quad (7)$$

in which k_1 is a constant and $f_p(x)$ is a function dependent only on the relative position x . However, the expression of $f_p(x)$ cannot be specified theoretically. As the first attempt, here we tentatively assume $f_p(x) = 1$. It should be noted that the point at $x = 0$ is a singularity under this assumption because $v_\phi(0)$ has a non-zero value that is not physically meaningful. We just ignore this singularity, and as will be seen in Sec.4.3, we prove that this assumption can be treated as an acceptable approximation. Then Eq.7 can be rewritten as

$$v_\phi(t, x) = v_p(t) = v_p(t_0) \frac{R(t_0)}{R(t)} \quad (8)$$

where the parameter $v_p(t)$ defines the poloidal speed of the plasma at the boundary of the flux rope in the direction of $\hat{\phi}$.

2.1.2 Parameters

In summary, Table 1 lists all the 11 free parameters in the velocity-modified cylindrical force-free flux rope model.

Besides, based on the cylindrical force-free flux rope assumption, we may derive more parameters, which have been also summarized in Table 1. It is straightforward to obtain the first two derived parameters, t_c and Θ . The next four parameters are derived as follows.

The axial magnetic flux, Φ_z , is given by

$$\Phi_z = \int_0^{2\pi} \int_0^R B_z r dr d\varphi = B_0 R^2 \kappa_1 \quad (9)$$

in which $\kappa_1 = \frac{2\pi}{x_0^2} \int_0^{x_0} x J_0(x) dx = 1.35$ and $x_0 = 2.41$ is the first zero point of Bessel function J_0 . The poloidal magnetic flux, Φ_φ , is given by

$$\Phi_\varphi = \int_0^l \int_0^R B_\varphi r dr dz = B_0 R l \kappa_2 \quad (10)$$

in which l is the length of the loop as denoted in Figure 1a and $\kappa_2 = \frac{1}{x_0} \int_0^{x_0} J_1(x) dx = 0.416$. The helicity, H_m , is given by [e.g., Berger, 2003]

$$H_m = \int_0^l \int_0^{2\pi} \int_0^R \mathbf{A} \cdot \mathbf{B} r dr d\varphi dz = B_0^2 R^3 l \kappa_3 \quad (11)$$

in which \mathbf{A} is a vector potential of \mathbf{B} and $\kappa_3 = \frac{2\pi}{x_0^3} \int_0^{x_0} x [J_0^2(x) + J_1^2(x)] dx = 0.701$. The magnetic energy, E_m , is given by

$$E_m = \frac{1}{2\mu} \int_0^l \int_0^{2\pi} \int_0^R B^2 r dr d\varphi dz = B_0^2 R^2 l \kappa_4 \quad (12)$$

in which $\kappa_4 = \frac{x_0}{2\mu} \kappa_3 = 6.72 \times 10^5 \text{ m H}^{-1}$.

We do not know the value of l , but we may assume that it is bounded between πL and $2L$, L is the heliocentric distance of the flux rope, as shown in Figure 1a. In practice, we let

$$l = \left(\frac{\pi + 2}{2} \pm \frac{\pi - 2}{2} \right) L \quad (13)$$

The uncertainty, $\frac{\pi-2}{2}L$, in the length of the flux rope will result in the uncertainty in Φ_φ , H_m and E_m . It should be noted that (1) the uncertainty here is not from the fitting procedure but the length of the flux rope, and (2) this treatment will underestimate the real length if the leg of an MC rather than its leading part was observed.

Considering the conservation of magnetic flux, we may infer from Eq.9 and 10 that

$$R \propto l \quad \text{or} \quad R \propto L \quad (14)$$

and consequently, the helicity is conserved too. Further, we may infer $E_m \propto L^{-1}$, suggesting that magnetic energy continuously decreases when an MC propagates away from the Sun. In this work, we calculate its initial value, E_{m0} , as listed in Table 1, which is the magnetic energy when the MC is only one solar radius away from the Sun, and the associated uncertainty of about $\pm 22\%$ comes from the uncertainty in l . Be aware that the decay index of the magnetic energy of an MC may not be -1 . The case study by Nakwacki *et al.* [2011], for example, has shown that the decay index for the MC observed by two spacecraft at 1 and 5.4 AU, respectively, on 1998 March is about -0.9 , a little bit slower than the expectation from our model. If the decay index varies from -0.9 to -1.1 , the extrapolated E_{m0} suffers an additional uncertainty of about ${}_{-71\%}^{+42\%}$, which we do not taken into account in our model.

The last derived parameter, χ_n , is used to evaluate the goodness-of-fit, which will be introduced in the following section.

2.1.3 Evaluation of the goodness-of-fit

Our fitting procedure is designed to fit the observed magnetic field, \mathbf{B}^o , and velocity, \mathbf{v}^o , together, which means that all the three components of \mathbf{B}^o and \mathbf{v}^o are used to constrain the model parameters. There are 11 free parameters, among which three of them are time-dependent (see Table 1) and can be determined by Eq.5, 6 and 8. Here, we use the first contact of the MC, t_0 , as the reference time. The detailed fitting process is as follows. First, by given a set of 11 free parameters, the imaginarily observational path relative to the axis of the flux rope can be derived from the orientation of the axis, (θ, ϕ) , the closest approach, d , the propagation velocity, (v_X, v_Y, v_Z) , and the expansion speed, v_e . Second, the coordinates of the observational path are then transformed from the GSE coordinate system to the MC frame, (r, φ, z) . In the MC frame, the three components of magnetic field along the path can be determined by Eq.1–3, in which the free parameters B_0 , R and H are involved, and the velocity can be calculated as $v_r \hat{\mathbf{r}} + v_\varphi \hat{\boldsymbol{\varphi}}$, in which v_r and v_φ are given by Eq.4 and 8. Third, we transform the derived magnetic field, \mathbf{B}^m , and velocity, \mathbf{v}^m , in the MC frame back to the GSE coordinate system, and evaluate the goodness-of-fit by calculating the normalized root mean square (rms) of the difference between the modeled and observed values of magnetic field and velocity, which is given as

$$\begin{aligned} \chi_n &= \sqrt{\frac{1}{2N} \sum_{i=1}^N \left[\left(\frac{\mathbf{B}_i^m - \mathbf{B}_i^o}{|\mathbf{B}_i^o|} \right)^2 + \left(\frac{\mathbf{v}_i^m - \mathbf{v}_i^o}{|\mathbf{v}_i^o| - v_{\text{ref}}} \right)^2 \right]} \\ &= \sqrt{\frac{1}{2} (\chi_{Bn}^2 + \chi_{vn}^2)} \end{aligned} \quad (15)$$

where N is the number of measurements, and v_{ref} is a reference velocity.

To find the best-fit, we use the IDL package, MPFIT (refer to <http://purl.com/net/mpfit>), to perform least-squares fitting [Markwardt, 2009; More, 1978]. The initial value of $B_0(t_0)$ is set to be the maximum value of the magnetic field strength during the interval of interest, the initial value of $R(t_0)$ is estimated as $\frac{1}{2} \bar{v}_X \Delta t$, in which Δt is the duration of the MC interval and \bar{v}_X is the mean value of the observed v_X , the initial value of the propagation velocity (v_X, v_Y, v_Z) is the mean value of the observed velocity, the initial value of the expansion speed is estimated from the slope of the observed radial velocity, and the initial value of the poloidal speed is set to be zero. For the free parameter H , we just fix its value to 1 or -1 by adding a loop in our fitting procedure. The elevation and azimuthal angles, θ and ϕ , are two most important free parameters. In order to get the best fitting result, we test the initial value of θ every 15° from -90° to 90° , and do the same thing for ϕ from 0° to 360° . Besides, we assume that the front and rear boundaries of an observed MC define the interval of the flux rope, and then the closest approach, d , could be uniquely determined based on the preset velocity and the axis orientation of the flux rope. In summary, we try 576 attempts of fitting (i.e., 576 sets of the initial values of the free parameters) for an MC, and select the case with the smallest value of χ_n as the best-fit.

The reference velocity in Eq.15 is used to adjust the weight of the velocity in evaluating the goodness-of-fit, and is set as

$$\frac{\max(|\mathbf{v}^o|) - \min(|\mathbf{v}^o|)}{\max(|\mathbf{v}^o|) - v_{\text{ref}}} = \frac{\max(|\mathbf{B}^o|) - \min(|\mathbf{B}^o|)}{\max(|\mathbf{B}^o|)} \quad (16)$$

Table 1: Parameters involved in the velocity-modified cylindrical force-free flux rope model*

Parameter	Explanation
Free parameters in the model	
$B_0(t)$	Magnetic field strength at the axis of the flux rope.
$R(t)$	Radius of the cross-section of the flux rope.
H	Handedness or sign of helicity, must be 1 (Right) or -1 (Left).
θ	Elevation angle of the axis of the flux rope in GSE.
ϕ	Azimuthal angle of the axis of the flux rope in GSE.
d	The closest approach of the observational path to the axis of the flux rope.
v_X	Propagation speed of the flux rope in the direction of $\hat{\mathbf{X}}$.
v_Y	Propagation speed of the flux rope in the direction of $\hat{\mathbf{Y}}$.
v_Z	Propagation speed of the flux rope in the direction of $\hat{\mathbf{Z}}$.
v_e	Expansion speed of the boundary of the flux rope in the direction of $\hat{\mathbf{f}}$.
$v_p(t)$	Poloidal speed at the boundary of the flux rope in the direction of $\hat{\phi}$.
Other derived parameters from the model	
t_c	The time when the observer arrives at the closest approach.
Θ	Angle between the axis of the flux rope and $\hat{\mathbf{X}}$ -axis.
Φ_z	Axial magnetic flux of the flux rope.
Φ_ϕ	Poloidal magnetic flux of the flux rope.
H_m	Magnetic helicity of the flux rope.
E_{m0}	Initial magnetic energy, i.e., the magnetic energy of the flux rope when it was one solar radius away from the Sun.
χ_n	Normalized root mean square (rms) of the difference between the modeled results and observations.

* See Sec.2.1 for the definition of coordinate systems, derivations of some parameters and other details.

If there was no reference velocity, χ_{Bn} and χ_{vn} may not have the same weight and cannot be inserted into one formula, because the dynamic range of the velocity is much different from that of the magnetic field. For example, assuming an MC interval during which the magnetic field varies from 5 to 35 nT and the velocity varies from 300 to 600 km s⁻¹, and at a given point $B^o = 25$ nT, $B^m = 20$ nT, $v^o = 500$ km s⁻¹ and $v^m = 450$ km s⁻¹, we can get that the relative error between the modeled and observed values in magnetic field is $\frac{5}{25} = 20\%$ and that in velocity is $\frac{50}{500} = 10\%$. The values of the relative errors are different. But if considering the range of 30 nT in magnetic field and the range of 300 km s⁻¹ in velocity, one can find that the relative difference between the modeled and observed values in magnetic field is the same as that in velocity. Thus the value of relative error depends on the dynamic range. To remove this effect, we use the reference velocity, which is 250 km s⁻¹ in the above case. The corrected relative error of the velocity becomes $\frac{50}{500-250} = 20\%$, the same as that of the magnetic field. After this treatment, χ_{Bn} and χ_{vn} can be fitted into one formula, Eq.15, to assess the goodness-of-fit.

The normalized rms, χ_n , has a definite meaning here. It measures the average relative error of modeled vectors, \mathbf{B} and \mathbf{v} , with both length and direction taken into account. It should be noted that the normalized rms here is different from those used in some studies. For example, in *Lepping et al.* [1990] and *Lepping et al.* [2006], \mathbf{B}^o and \mathbf{B}^m are normalized by the strength of themselves, and that rms merely reflects the average deviation of vector directions; while in *Marubashi et al.* [2012], \mathbf{B}^o and \mathbf{B}^m are normalized by the maximum value of observed B during the whole interval of the flux rope, which might imply that a stronger MC has a smaller value of rms.

2.2 Events and model testing

The MC list compiled by *Lepping et al.* [2006] is the basis of this study, and hereafter we call it Lepping list (see http://lepmfi.gsfc.nasa.gov/mfi/mag_cloud_S1.html; the list including the fitted parameters are kept being updated until 2011 December 13). We use this list not only because it is well established but also because we can test the procedure of our model by comparing our fitting results with *Lepping et al.* [2006] results. There are a total of 121 MCs in the list. The start time, end time and model-derived parameters are all given in the list. The goodness-of-fit is estimated by Q_0 , which is 1, 2 or 3 for good, fair and poor, respectively. Our study only considers the MCs in the first two categories. It is noticed that there are large data gaps in the published Wind data during 2000 July 15 – 16. Their event No.45 and 46 are in that period, and are therefore removed from our study. Besides, the event No.85 in their list was studied by *Dasso et al.* [2009], and is believed to consist of two MCs. Thus we discard this event too. Finally, a total of 72 events are available for our study as listed in Table 2–4 in Appendix B.

To test our procedure, we switch off the velocity option in our model, and compare the fitted parameters with those given in Lepping list. When fitting an observed MC with our model, we use the time-resolution of the Wind data as the same as that indicated in the list, which is 15 minutes for some events and 30 minutes for others. The front and rear boundaries of the MCs given in Lepping list are used and fixed in our model. It is different from the procedure taken by *Lepping et al.* [2006], in which the preset boundaries may be modified by their model. The difference between their fitted and observed boundaries is evaluated by the parameters,

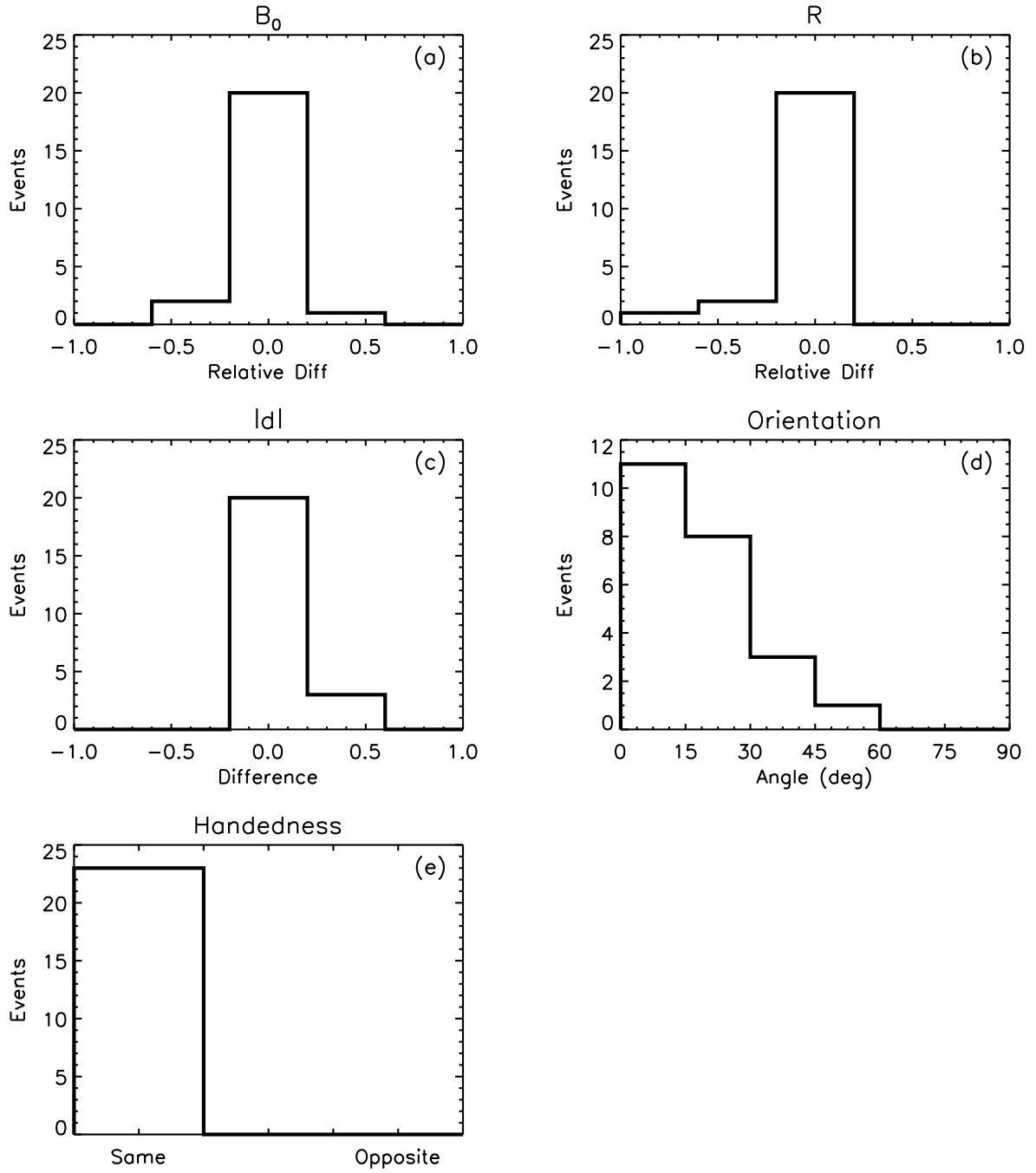


Figure 2: Histograms showing the differences of the values of fitting parameters between the Lepping's model and our model without velocity measurements taken into account. From top to bottom and left to right, there are the relative difference of the magnetic field strength (B_0) at the MC's axis between the two models, the relative difference of the radius (R), the difference of the closest approach $|d|$, the acute angle between the MC's axes derived from the two models, and the difference of the handedness.

ck and asf, given in their list (see Eq.7 and 9 in *Lepping et al.* 2006 for their definitions). Larger values of ck and asf mean larger difference. Thus to make a mostly reliable comparison, we further tentatively exclude events whose ck or asf is larger than 10%, that results in a sample of 23 events. It should be noted that those excluded events will be included again in the next section though they are not used for testing our procedure here.

The parameters characterizing the configuration and strength of an MC are compared, which are H , B_0 , R , d , and orientation (θ and ϕ) of an MC. Figure 2 shows the differences of the values between the parameters from our and *Lepping et al.* [2006] procedures. It is found that both of them suggest the same sign of helicity, H , for each MC (Fig. 2e). For B_0 and R , we calculate the relative difference, $\frac{f-f_L}{f_L}$, where f is from our results and f_L from Lepping list. Our procedure gets very similar results with Lepping list (Fig.2a and 2b). There are only 3 events, in which the relative difference in B_0 and R is outside of $\pm 20\%$. For d , we do not use the above equation to calculate the relative difference, because d is a ratio of the closest approach to the radius of the flux rope and its value could be zero which may cause the value of the relative difference to be extremely large. Instead, we directly use the difference of absolute values of them, $|d| - |d_L|$. A good agreement also can be obtained between the two procedures (Fig.2c). The two parameters θ and ϕ , which define the orientation of a flux rope's axis, are compared together. We calculate the angle between the orientation derived by our procedure and that given in Lepping list. It is found that the angle is smaller than 60° , and for most (19 out of 23) events, the angle is less than 30° . Overall, the comparison shows that our procedure can almost reproduce the results derived by *Lepping et al.* [2006], confirming the validity of our procedure.

Now we switch on the velocity option, and apply the model to the 72 high-quality events in Lepping list. The time-resolution of the data input into our model is set to 10 minutes. All the parameters derived from our fitting procedure of these events have been listed in Table 2–4 in Appendix B for reference. In the following two sections, we will evaluate the effects of velocity on the goodness-of-fit, and show the statistical properties of plasma motion.

3 Effects of velocity on the fitting results

The goodness-of-fit is evaluated by the average relative error, χ_n , given by Eq.15. For all the 72 events, the distribution of χ_n has been displayed in Figure 3a. It is found that the values of χ_n are all less than 60%, and on average, χ_n is about 28%. Further, the comparison between the cases of velocity-on and velocity-off shows that considering velocity may get the value of χ_{Bn} larger or smaller (see Fig.3b). As examples, Figure 4a and 4b show two cases; for one of them the fitting to the magnetic field gets worse, and for the other, the fitting looks better. In a typical MC measurements, a declining velocity means the expansion of the MC and as a consequence, the magnetic field strength of the MC should decrease as well. The former case does not follow the picture. The strongest magnetic field appeared in the rear part of the MC, but the velocity profile indicates a clear expansion, suggesting that the strongest magnetic field should appeared in the front part of the MC. The fitting without ve-

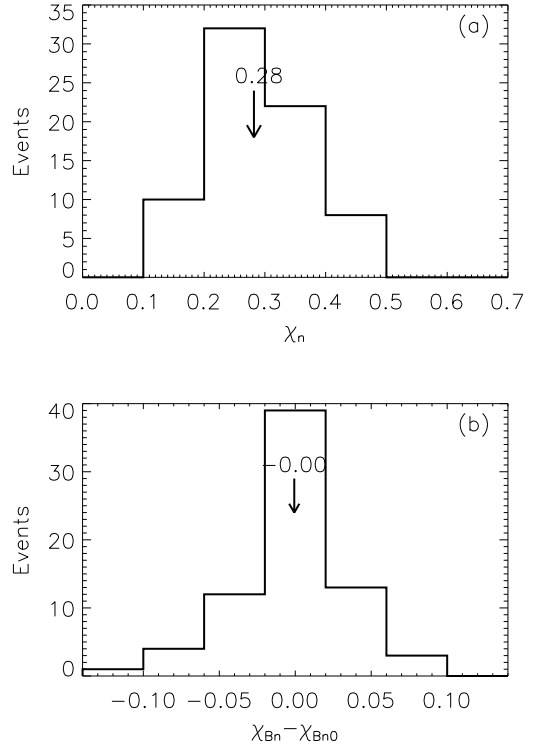


Figure 3: The distributions of normalized rms, which show the goodness-of-fit. (a) the normalized rms (χ_n) calculated from both magnetic field and velocity, and (b) the difference of the normalized rms in magnetic field between the model results with velocity-on (χ_{Bn}) and velocity-off (χ_{Bn0}).

locity being taken into account gives the blue dashed curves, which match the observed magnetic field much better than red solid curves given by our velocity-modified model. The latter case is a typically expanding MCs, and therefore the magnetic field is fitted better.

Except those velocity-related parameters (which will be presented in the next section), the parameters of MCs derived from our velocity-modified model are summarized in Figure 5. For the magnetic field strength at the MC axis, most events fall into the range from 10 to 30 nT with a median value of about 16 nT. For the radius, all the MCs are less than 0.25 AU, and its median value is about 0.09 AU. Note, the values of the above two parameters are all adopted at the time, t_c , when the observer arrives at the closest approach to the MC axis. The angle between the MC axis and the Sun-spacecraft line, Θ , could be any value from 0° to 90° . The most probable angle is within $45^\circ - 75^\circ$, and the median angle is about 53° . It suggests that observed MCs are more likely to transversely cross over the observer. The elevation angle of the MC axis tends to be small, with a median value of about 15° , implying low tilt angles of flux ropes when they erupted from the Sun.

Further by using the total length of the flux rope, l , given by Eq.13, we estimate that the total magnetic flux, which includes axial flux and poloidal flux, is on the order of 10^{21} Mx with the median value of about 4.1×10^{21} Mx. The distributions of the axial flux and poloidal flux are also indicated by dotted and dashed lines (Fig.5e). Their median values are 0.4×10^{21} and 3.6×10^{21} Mx, respectively. The estima-

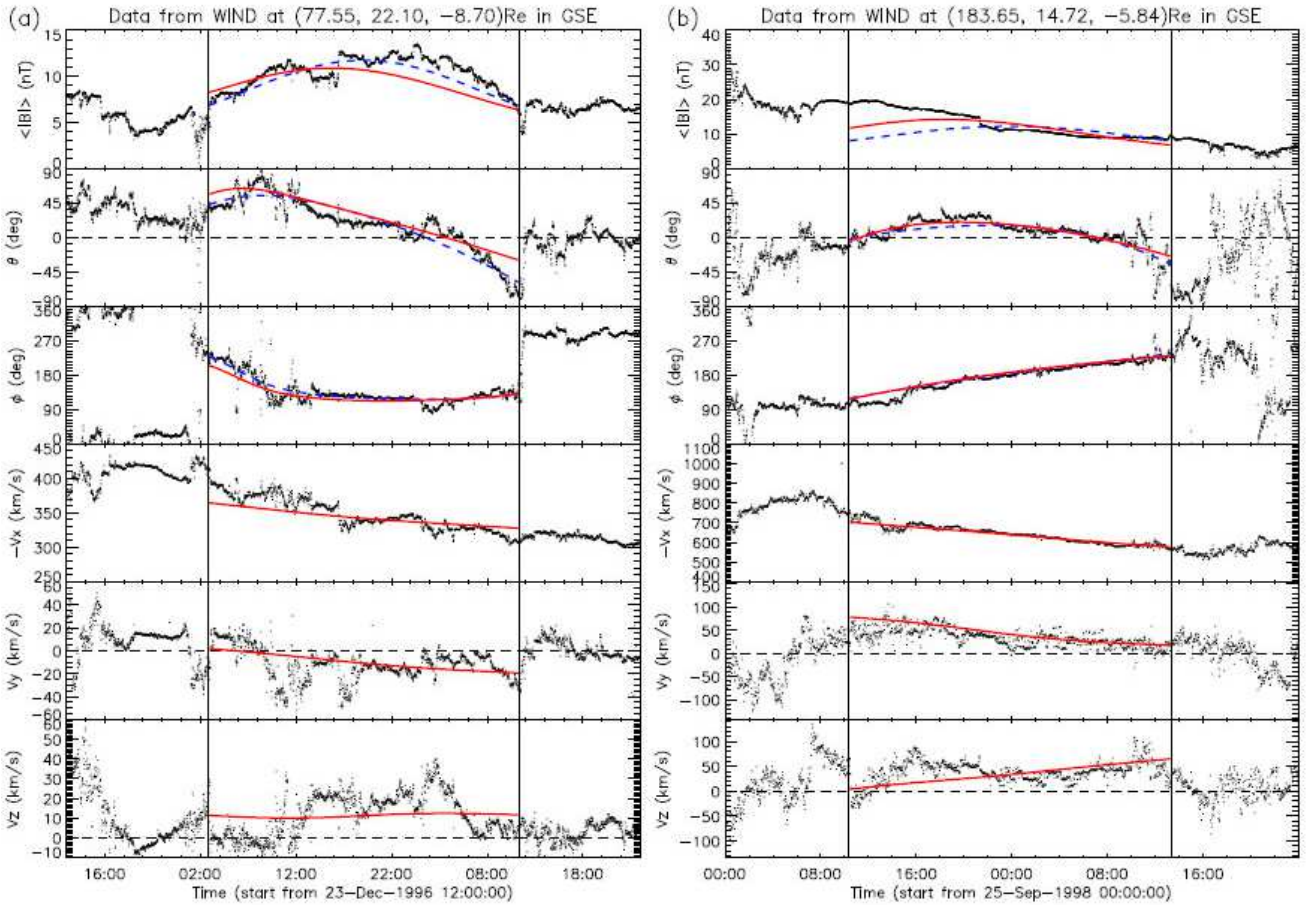


Figure 4: Two cases showing the comparison of the fitting results of our model with velocity-on (the red lines) and off (the blue dashed lines). Case (a) shows that the fitting results become worse when the velocity is taken into account, and Case (b) shows an opposite situation. In both cases, from the top to bottom, the panels are total magnetic field strength, elevation and azimuthal angles of magnetic field vector and three components of bulk velocity of solar wind plasma, respectively. The two vertical lines mark the front and rear boundaries of the MCs.

tion of the magnetic flux of MCs were made before by, e.g., *Dasso et al.* [2005], *Dasso et al.* [2007] and *Nakwacki et al.* [2008]. In *Dasso et al.* [2005], for example, eight well-defined MCs were investigated and it was found that the axial flux is around 0.4×10^{21} Mx, highly consistent with the result obtained here. Our results are also roughly in agreement with previous studies about the magnetic flux of MCs and reconnection flux of solar eruptions by, e.g., *Qiu et al.* [2007].

The helicity is shown in Figure 5f and 5h. The number of right-handed MCs is almost equal to the number of left-handed MCs, and the absolute value of the helicity is about 2.05×10^{42} Mx² on average. For the 8 events studied by *Dasso et al.* [2005], the helicity per unit length is about 1×10^{42} Mx²/AU. According to Eq.13, the helicity in their study is about 2.57×10^{42} Mx², consistent with the average value we obtained here. Moreover, the initial magnetic energy is found to be about 2.84×10^{31} erg, nearly one order higher than the kinetic energy of a typical CME, which is about $10^{29} - 10^{30}$ erg [e.g., *Vourlidis et al.*, 2010], even considering the uncertainty in the decay index when we extrapolate the initial magnetic energy.

Nakwacki et al. [2008] compared the static and expansion models and found that the modeled values of the MC pa-

rameters are not changed too much. Here we consider not only the expansion but also other types of motion. Will the values of parameters change more significantly? By comparing the values of the fitting parameters obtained from the velocity-modified and non-velocity models as shown in Figure 6, we find that the values are more or less changed, but not too significantly except the orientation. The magnetic field strength is almost unaffected. For the radius, about 13% (9 out of 72) of the events get a smaller value after velocity is taken into account, and about 10% of the events get a larger value. For the closest approach, the velocity-modified model believes that the observer should be slightly farther away from the MC axis for 8 events and closer for only 4 events. The largest difference appears in the orientation. There are about 40% of the events, for which the orientation is changed by more than 15°, and particularly, there are 6 events with the difference in orientation larger than 45°. Besides, for two cases, the handedness is also changed.

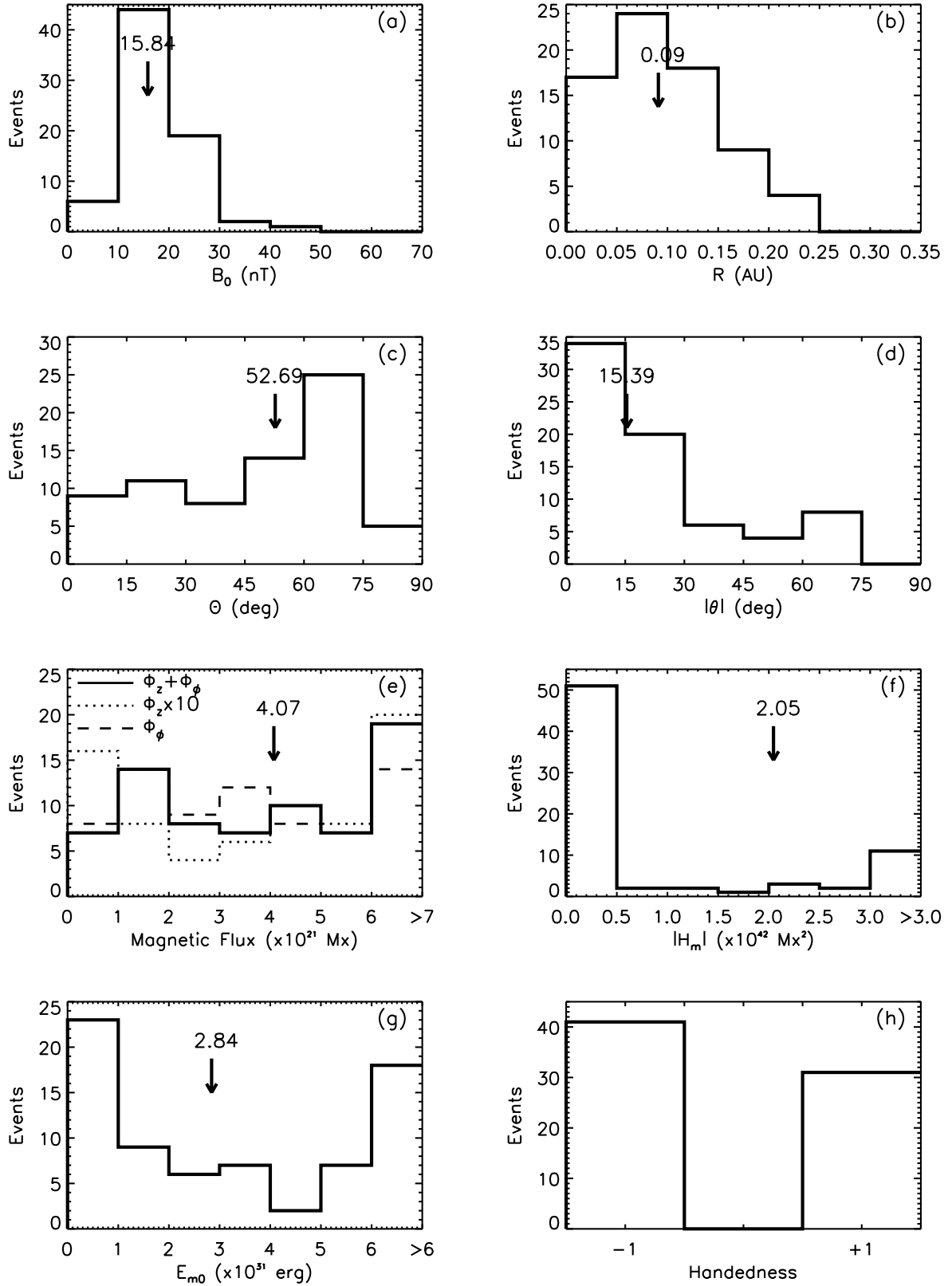


Figure 5: The distributions of the values of the fitting parameters from the velocity-modified model for 72 MC events. From the top to bottom and left to right, the panels show the magnetic field at the MC's axis (B_0), the radius the MC's cross-section (R), the acute angle between the axis and the Sun-spacecraft line (Θ), the absolute value of the elevation angle of the axis ($|\theta|$), the total magnetic flux ($\Phi_z + \Phi_\phi$), the unsigned helicity ($|H_m|$), the initial magnetic energy (E_{m0}) and the handedness (H). The median values of these parameters are indicated by the arrows.

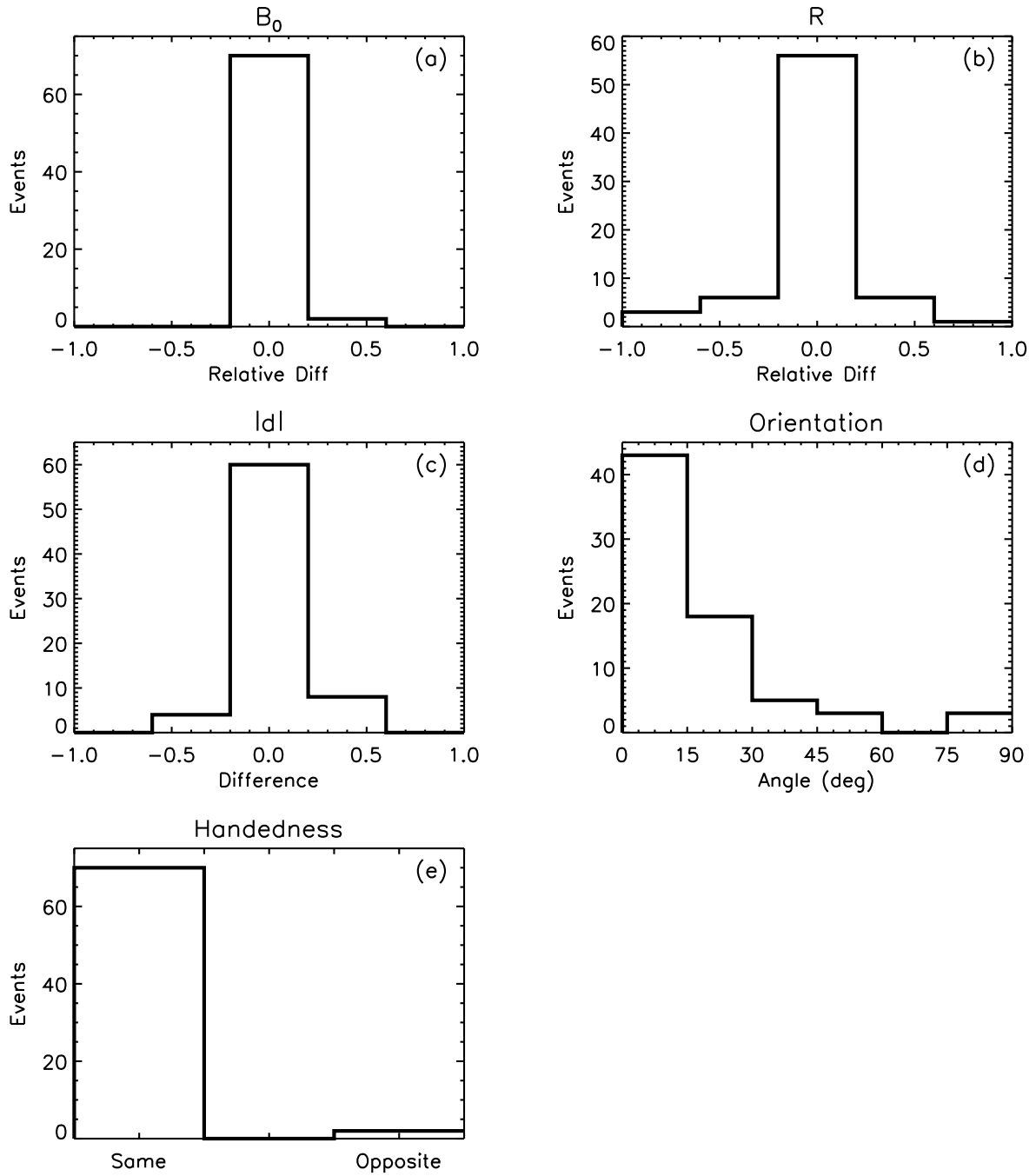


Figure 6: Histograms showing the differences of the values of fitting parameters between our model with and without velocity measurements taken into account. The arrangement is as the same as that in Fig. 2.

4 Statistical properties of plasma motion

4.1 Linear propagating motion

One important implication to consider the velocity in fitting procedure is to reveal the properties of the plasma motion of MCs. First, we investigate the axial component, v_{axis} , and perpendicular component, v_{perp} , of the linear propagating motion of an MC. The former is a velocity along the MC's axis, i.e., in the z -direction of the MC frame, and the latter is a velocity perpendicular to the radial direction, i.e., the Sun-spacecraft line, $v_{perp} = \sqrt{v_Y^2 + v_Z^2}$.

The ratio of the axial velocity to the radial velocity, $-v_{axis}/v_X$, as a function of the orientation of the MC's axis is shown in Figure 7a. A very nice correlation between them could be found. When the axis is almost aligned with Sun-spacecraft line, the absolute value of v_{axis} is almost equal to that of v_X , and when the axis becomes more and more perpendicular to the Sun-spacecraft line, v_{axis} approaches zero. It well follows the cosine function as indicated by the solid line. The small deviation away from the cosine function is no more than $0.06v_X$, which corresponds to a very small speed on the order of 10 km s^{-1} . This result suggests that the apparent axial velocity is mostly a consequence of the propagation of the MC though an insignificantly pure-axial flow might exist inside an MC.

The distribution of v_{perp} is given in Figure 8. Panel (a) shows that except 6 events, all the other events have a perpendicular velocity less than 60 km s^{-1} , and Panel (b) suggests that in 61 (about 85% of) events the perpendicular velocity is no more than 10% of radial velocity. A noteworthy thing is that some events have a significantly perpendicular velocity with respect to the radial velocity. The MC shown in Figure 4b is an example, which occurred on 1998 September 25. Our model infers that the orientation of the MC axis is $\theta = 60^\circ$ and $\phi = 196^\circ$, and the plasma motion of the MC is the combination of the linear motion at $-624, 95$ and 50 km s^{-1} in \hat{X} , \hat{Y} and \hat{Z} directions and the expansion and poloidal motion at 90 and -23 km s^{-1} , respectively.

Considering the expansion of the whole looped structure as shown in Figure 1b and that there is no significantly pure-axial flow inside an MC, one may find that a significantly perpendicular velocity may be present if not the front part (or the apex) but the flank (or the leg) of the MC was detected locally. Which part of a looped MC is detected by spacecraft could be roughly inferred from the orientation of the MC axis. We think that the apex of an MC is encountered if the inferred axis of the MC is almost perpendicular to the Sun-spacecraft line, and the leg is encountered if the axis is almost parallel to the Sun-spacecraft line. Thus, if the expansion of the whole looped structure was the reason of the presence of the perpendicular velocity, we may expect a very small perpendicular velocity for those apex-encountered events. Figure 7b shows the scatter plot of $-v_{perp}/v_X$ versus Θ . Obviously, there is no dependence of the perpendicular velocity on the axis orientation. For those events with Θ close to 90° , the perpendicular velocity could be larger than 10% of the radial velocity. Thus, there must be some other reasons for the significantly perpendicular motion.

We think that the presence of a significantly perpendicular velocity might be an in-situ evidence of deflected propagation of a CME in interplanetary space [e.g., Wang et al.,

2004, 2014; Lugaz, 2010; Isavnin et al., 2014]. The positive value of v_Y of the 1998 September 25 event suggests an eastward deflection in the ecliptic plane. This is in agreement with the proposed picture by Wang et al. [2004] that a CME faster than background solar wind will be deflected toward the east. If a CME propagated in interplanetary space with a perpendicular velocity at a tenth of the radial velocity, i.e., $-\frac{v_{perp}}{v_X} = \frac{1}{10}$, the deflection angle is then given by

$$\int_{t_0}^{t_1} \frac{v_{perp}}{L} dt = \int_{L_0}^{L_1} -\frac{v_{perp}}{v_X L} dL = \int_{L_0}^{L_1} \frac{1}{10L} dL \quad (17)$$

Assuming $L_1 = 1 \text{ AU}$ and L_0 less than 5 solar radii, we can estimate that the deflection angle is more than 20° . This is quite consistent with our recent case study of a CME, which was found to be deflected by more than 20° on its way from the corona to 1 AU [Wang et al., 2014]. Alternatively, the perpendicular velocity might also be the result of the rotation of the whole structure of a CME with respect to the radial direction in interplanetary space, just as the rotation in the middle and outer corona [e.g., Yurchyshyn et al., 2009; Vourlidas et al., 2011; Isavnin et al., 2014].

4.2 Expanding motion

The distribution of the expansion speed is shown in Figure 9a. It is noteworthy that a significant fraction (about 26%) of the events experienced a contraction process with a median value of about 12 km s^{-1} . We check the large contraction events having $v_e < -20 \text{ km s}^{-1}$, and find unsurprisingly that they were all caused by the overtaking of faster solar wind stream, as illustrated by the example in Figure 10. In that event, the solar wind speed after the trailing edge of the MC is much larger than that before the leading edge, which cause the magnetic field strength increase with time, and reach the maximum near the rear boundary. Under this circumstance, the MC cannot expand freely, but will be compressed by ambient solar wind. Our model suggests that the contraction speed of the MC is about 27 km s^{-1} .

For the rest of the events suggested to be expanding at 1 AU, the median speed is about 21 km s^{-1} . The expansion substantially depends on the balance between the internal and external forces. The internal force is partially characterized by magnetic field strength. Figure 9b shows the correlation between v_e and B_0 . The black dashed line is the linear fitting to all the data points and the blue solid line is the linear fitting to the data points of $v_e > 0$ (blue dots). A weak correlation could be found, but it is not significantly different between all data points and data points of $v_e > 0$. The correlation coefficient is not so high, because the external condition is not considered. With the increasing distance away from the Sun, both the magnetic and thermal pressures in the solar wind usually decrease. It will consequently cause the unbalance between the internal and external forces, which drives a CME/MC expanding. Thus we may expect that the expansion speed should be correlated with propagation speed. As shown in Figure 9c, there does exist a stronger correlation between v_e and v_X for expansion events. The correlation coefficient is about 0.55. It is consistent with the previous result by, e.g., Démoulin and Dasso [2009a] that rapid decrease of the total solar wind pressure with heliocentric distance is the main driver of the MC ex-

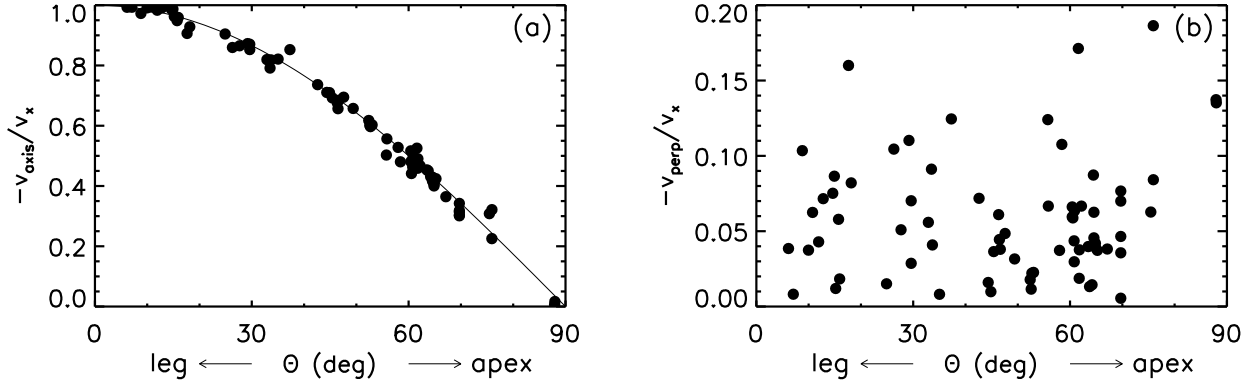


Figure 7: (a) The axial velocity and (b) the perpendicular velocity as a function of the angle between the MC’s axis and the Sun-spacecraft line. Both the velocities are normalized by the value of radial propagation velocity. A small value of Θ means an encounter of the leg of an MC and a large value of Θ means an encounter of the apex of an MC.

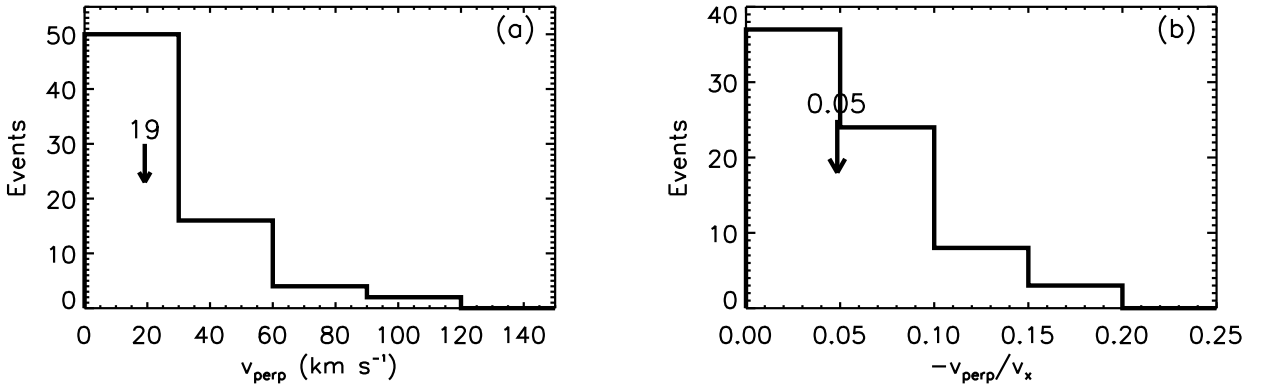


Figure 8: Distributions of (a) the propagation velocity perpendicular to the radial direction, i.e., the Sun-spacecraft line and (b) its value relative to the radial propagation velocity. Median value is indicated by the arrow in each panel.

pansion. Similar results could also be found for the events in the inner and outer heliosphere [Gulisano et al., 2010, 2012].

On the other hand, the MC expansion could be classified as self-similar expansion, overexpansion and underexpansion. Note, the term ‘self-similar’ here only refers to that the radius, R , of an MC evolves proportionally to the distance L , which is a subset of that defined in Sec.2.1 where ‘self-similar’ means that not only the size but also the internal plasma parameters of the MC evolve self-similarly. Imaging data have suggested that most CMEs undergo a self-similar expansion in the outer corona [e.g., Schwenn et al., 2005], but whether or not they maintain the self-similar expansion in interplanetary space? To measure the expansion rate of MCs, Gulisano et al. [2010] used a dimensionless quantity $\zeta = \frac{\Delta u_x}{\Delta t} \frac{L}{v_x}$, in which Δu_x is the difference of the measured solar wind speed along the Sun-spacecraft line between the front and rear boundaries of an MC. They found that the value of ζ is about 0.7 after analyzing all the MCs observed by Helios spacecraft. Considering Δu_x is a proxy of the expansion speed of an MC and $v_x \Delta t$ approximates the size of the MC, we may infer that $\zeta \approx \frac{v_e}{-v_x} \frac{L}{R}$, and $\zeta < 1$ means an underexpansion. Thus, the parameter, ζ , has the same physical meaning of the power index, n , appearing in the power law of the heliocentric distance dependence of the CME/MC size

[e.g., Bothmer and Schwenn, 1998; Démoulin et al., 2008; Savani et al., 2009], namely $S = cL^n$, where S is the MC size and c is a constant. Bothmer and Schwenn [1998] found $n \approx 0.78$ and Démoulin et al. [2008] gave $n \approx 0.8$. Here we use model derived parameters to investigate the expansion rate again. Since all the MCs in this study located at 1 AU, we have $L = 1$ AU. Figure 9d shows the plot of $-v_e/v_x$ versus R/AU . The self-similar expansion is given by the dashed line. The data points above the line suggest an overexpansion, and those below the line a underexpansion. By considering a 20% uncertainty as indicated by the two dotted lines, we find that only 21% of the events underwent a nearly self-similar expansion, and 62%/17% of the events have and expansion rate lower/larger than 0.8/1.2. By using a function of $\frac{v_e}{-v_x} = \zeta \frac{R}{1\text{AU}}$ to fit the all these data points as indicated by the solid line, we get $\zeta \approx 0.6$ on average, generally consistent with that obtained by, e.g., Bothmer and Schwenn [1998], Démoulin et al. [2008] and Gulisano et al. [2010], if the uncertainty is considered. A possible reason of why the expansion rate is significantly below unity is that the MCs are perturbed by ambient solar wind and/or other transients as shown in observational statistics [Gulisano et al., 2010], which may cause the external pressure surrounding the MC decreasing with distance more slowly than usual. The numerical simulations by, e.g., Xiong et al. [2006, 2007], Lugaz et al. [2013] also suggested that CME-CME interac-

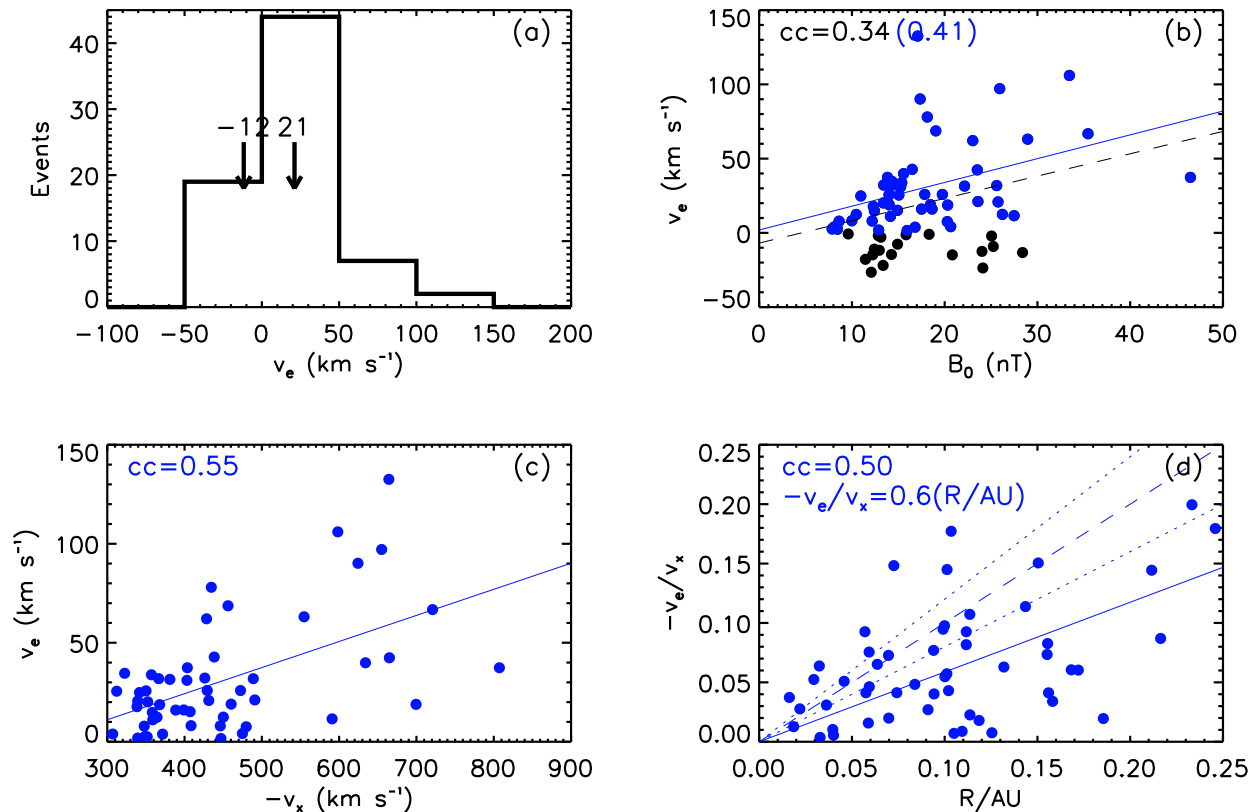


Figure 9: (a) Distribution of the expansion speed. The two arrows indicate the mean values for negative and positive expansion speeds, respectively. (b) Scatter plot showing the correlation between the expansion speed and magnetic field strength. Blue dots indicate the expansion events and black dots the contraction events. The black dashed and blue solid lines are the linear fitting to the all data points and the blue data points, respectively. (c) Scatter plot showing the correlation between the expansion speed and the radial propagation speed. The line gives the linear fitting result. (d) Scatter plot showing the correlation between the expansion speed in units of the radial propagation speed and the MC’s radius in units of AU. The solid line gives the fitting result by a function of $y = ax$ as marked in the upper-left corner of the panel. The dashed line indicates the self-similar expansion, i.e., R evolving proportionally to L , and the two dotted lines give the 20% uncertainty. For the panel (c) and (d), only expansion events are included.

tion may affect the expansion rate of the preceding CME.

It should be noted that in our model the expansion speed is derived based on the measured solar wind velocity along the Sun-spacecraft line and therefore the expansion speed here is more likely to reflect the radial expansion rather than lateral expansion. Lots of studies have shown that the cross-section of a CME will more or less distorted from the circular shape to a pancake shape [e.g., *Riley et al.*, 2003; *Riley and Crooker*, 2004; *Owens et al.*, 2006], suggesting that the lateral expansion is probably faster than the radial expansion. Thus, the lateral expansion may probably still be self-similar as that in the outer corona though the radial expansion is not.

One may notice that our model implies that $R \propto L$, meaning a self-similar expansion (see Sec.2.1.2). It is inconsistent with the result here. This inconsistency may come from various sources, e.g., the assumption of the magnetic flux and/or helicity conservation, the assumption of $L \propto l$, and the assumption of the uniformly straight cylindrical geometry. It will consequently affect the values of some derived parameters, e.g., Φ_φ , H_m and E_m . Although such an inconsistency exists, we think that the values of these derived parameters

still could be treated as a first-order approximation.

4.3 Poloidal motion

The distribution of poloidal speed is shown in Figure 11. The median value is about 10 km s^{-1} . By comparing the poloidal speed with other parameters, we cannot find any significant correlation among them (all the correlation coefficients are no more than 0.40). Obviously, the poloidal speed, if any, is less significant than the expansion speed on average. This fact may cause the observational signature of the poloidal motion in an MC unclear. To most clearly show the poloidal motion, we choose the events without significant expansion and convert the velocity into the Cartesian frame, (x', y', z') , of the MC (see Sec.2.1.1 for the definition of the coordinates). A nice example is shown in Figure 12, which was observed on 2009 October 12. The two vertical lines mark the beginning and the end of the MC, and the fitting results are given by the red curves in Figure 12a. According to the modeled parameters, the path of Wind spacecraft in the MC frame is shown in Figure 12e. Along the path from the beginning to the end of the MC, the rotation of the mag-

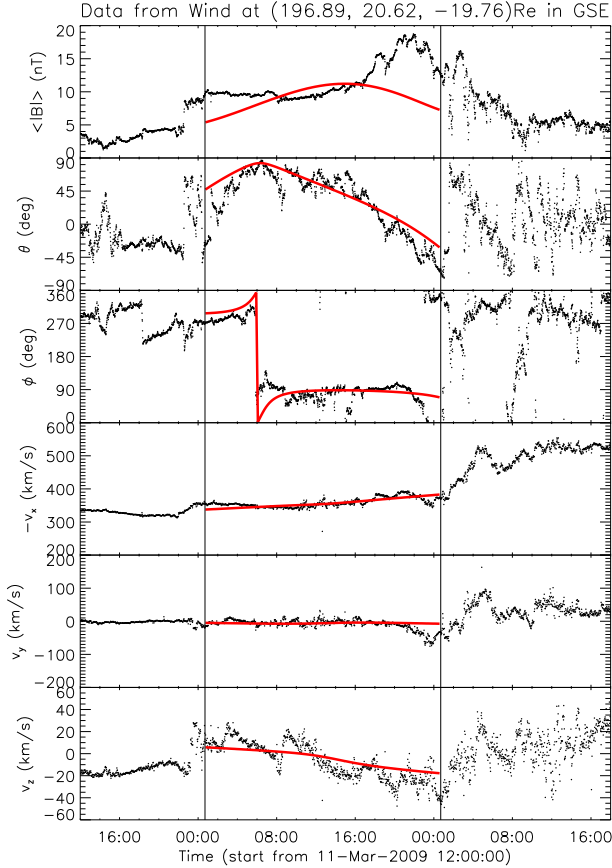


Figure 10: An example of contraction events. The arrangement is as the same as that in Fig. 4.

netic field vector is well presented in both the (x', y') and (y', z') planes (see Fig.12b and 12c). The color-coded dots are observations and the color-coded lines are fitting curves. More interestingly, the poloidal motion is evident in the MC frame (Fig.12d). In this event, the expansion speed is almost zero and the poloidal speed is about -31 km s^{-1} at time of t_c . Figure 13 shows another event on 2003 March 20, in which the modeled poloidal speed is 58 km s^{-1} , more significant than the modeled expansion speed of about 19 km s^{-1} , and therefore the poloidal motion can be also recognized in observations.

Based on the model, we could expect that the data points of velocity will form an arc which is symmetric about the axis of $v_{y'} = 0$ if the poloidal motion was significant and dominant in an MC. The above two cases just show the pattern. However, the arc's symmetrical axis will change to $v_{x'} = 0$ if the expansion was significant and dominant. Figure 14a roughly shows the case, which was observed during 1998 November 8 – 10 and the values of v_e and v_p are 69 and -8 km s^{-1} , respectively. If both expansion and poloidal motion are significant, the 'symmetric' axis will rotate, and the velocity data points may deviate slightly from a symmetric distribution. The 2001 April 4 – 5 event shown in Figure 14b is an example to show the change.

It should be noted that $f_p(x)$ in the equation of poloidal speed (Eq.7) is assumed to be unity. Whether or not is this assumption reasonable? We check it by investigating the cor-

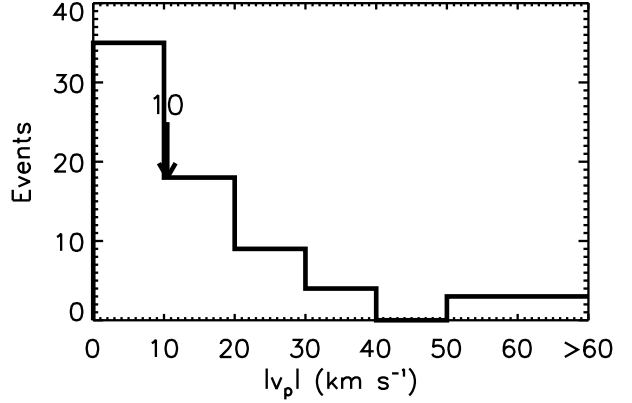


Figure 11: Distribution of the poloidal speed.

relation between $f_p(x) = \frac{v_\phi R}{k_1}$ and x as shown in Figure 15. v_ϕ is derived from velocity measurements in the MC frame, and R are obtained from model results. k_1 is an unknown constant, that may change from one event to another. We determine the value of k_1 by making the value of $f_p(x)$ of most data points around unity. All the data points of the 72 events are plotted together to show the statistical trend (Fig.15a). The red diamonds in the figure are the mean values of the data points in the bins with a horizontal size of 0.2, and the error bars indicate the standard deviations. The blue line gives $f_p(x) = 1$. It is clear that data points are generally distributed around the blue line no matter which value x is, though a large scattering is evident, suggesting that $f_p(x) = 1$ is an appropriate assumption from the view of statistics.

However, the form of $f_p(x)$ is case dependent. Is the assumption of $f_p(x) = 1$ generally appropriate for an individual MC? It is further checked in Figure 15b–15h, in which the dependence of $f_p(x)$ on x for 7 selected MCs are presented. These 7 MCs are selected for investigation because (1) the derived poloidal speed is significant, larger than 10 km s^{-1} , and (2) the closest approach is smaller than $0.5R$ so that there is a complete scan of x . For different events, the pattern is indeed different. Figure 15b and 15h suggest a general increase of $f_p(x)$ with increasing x , Figure 15d and 15f show that $f_p(x)$ has a unimodal distribution, and Figure 15c, 15e and 15g show a reversed unimodal distribution of $f_p(x)$. If considering the errors, we find that $f_p(x)$ is almost independent on x for all the cases except the last one (Fig.15h). Even for the last case, $f_p(x)$ is almost invariant for $x > 0.4$. Thus, based on the above analysis, we may treat the simplest assumption, $f_p(x) = 1$, as an acceptable approximation.

5 conclusions and discussion

In this paper, we present a velocity-modified cylindrical force-free flux rope model in details. Both observations of in-situ magnetic field and plasma velocity are taken into account by our model to derive the geometrical and kinematic parameters of MCs, which have been summarized in Table 1. The validity of our fitting procedure and the effect of velocity on the fitting results are checked through the Lepping list. It is found that the values of the modeled radius and orien-

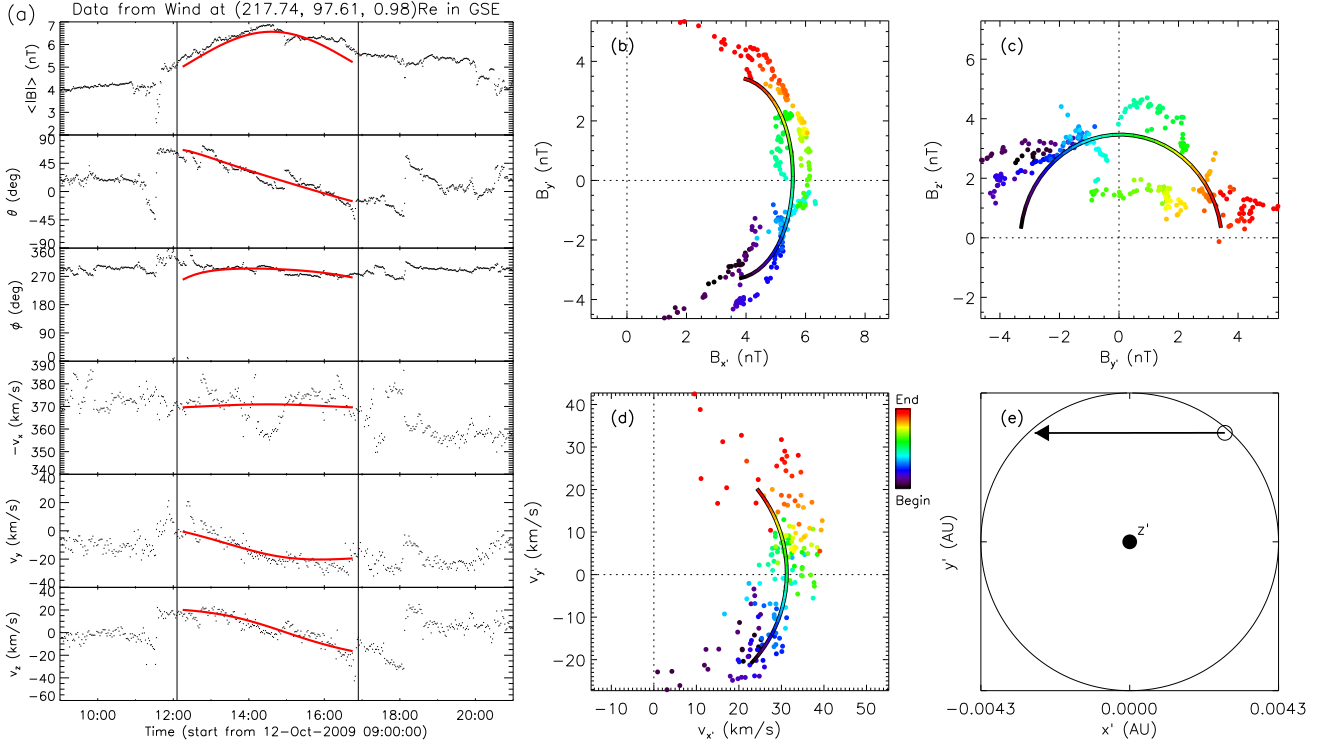


Figure 12: An MC observed on October 12, 2009. (a) The fitting results of the velocity-modified model. The arrangement of the panels is as the same as that in Fig. 4. (b) and (c) The magnetic field components in the (x', y') and (y', z') plane of the MC frame, respectively. The data points are color-coded, indicating the time from the beginning (black, corresponding to the first vertical line in the plot (a)) of the MC to the end (red, corresponding to the second vertical line in the plot (b)). The color-coded lines are the fitting results. (d) The velocity in the (x', y') plane. (e) The derived cross-section of the MC (the circle) and the observational path (the arrow). See main text for more details.

tation of an MC and the closest approach are more likely to be changed significantly if the velocity is considered. In our sample, the radius changes its value by more than 20% in 22% of the cases, orientation changes by more than 30° in 15%, and the closest approach changes by more than 20% in 17%. In a few cases, the handedness may also be changed. We then obtain the statistical properties of MCs, including the magnetic field strength, radius, orientation, magnetic flux, helicity and initial magnetic energy, which have been summarized in Figure 5. Furthermore, some findings about the plasma motion of MCs are obtained.

1. The linear propagation velocity may not be along the radial direction. The value of the non-radial component of the propagation velocity could be more than 10% of radial speed in some cases, which constitutes the direct evidence of the deflected propagation and/or rotation of a CME in interplanetary space.
2. As previous studies have shown (see Sec.4.2), the expansion speed is correlated with the radial propagation speed with a coefficient of about 0.55, and most MCs did not undergo a self-similar expansion at 1 AU in radial direction, i.e., the radius is not evolving proportionally to the heliocentric distance. In our statistics, 62%/17% of MCs underexpanded/overexpanded with an expansion rate $< 0.8/ > 1.2$, and on average the expansion rate is about 0.6.

3. The poloidal motion is not as significant as expanding motion generally, but does exist in some cases. Its speed is on the order of 10 km s^{-1} at 1 AU.

The last point is of particular interest. Considering the possible presence of small pure-axial velocity (see Sec.4.1), there may exist helical plasma motion following the helical magnetic field lines of an MC, which is worth to be investigated further. No matter how the plasma elements move inside the MC, the presence of the poloidal motion means that MCs may carry non-zero angular momentum. We think that there are at least three possible causes of the angular momentum.

The first is that the angular momentum is generated locally through the interaction with ambient solar wind. If there is the velocity difference between the solar wind and an MC, the solar wind plasma would stream around the MC body. The viscosity or some other processes may cause the poloidal motion inside the MC. If this is true, we would expect that the poloidal speed, v_p , is stronger at the periphery of the flux rope and therefore the absolute value of the derived v_p is positively correlated with the closest approach, d . Our statistical study suggests that there is a weak correlation between them as shown in Figure 16a; the correlation coefficient is about 0.4. This result implies that the local solar wind interaction perhaps is probably a factor for the poloidal motion but not the only one.

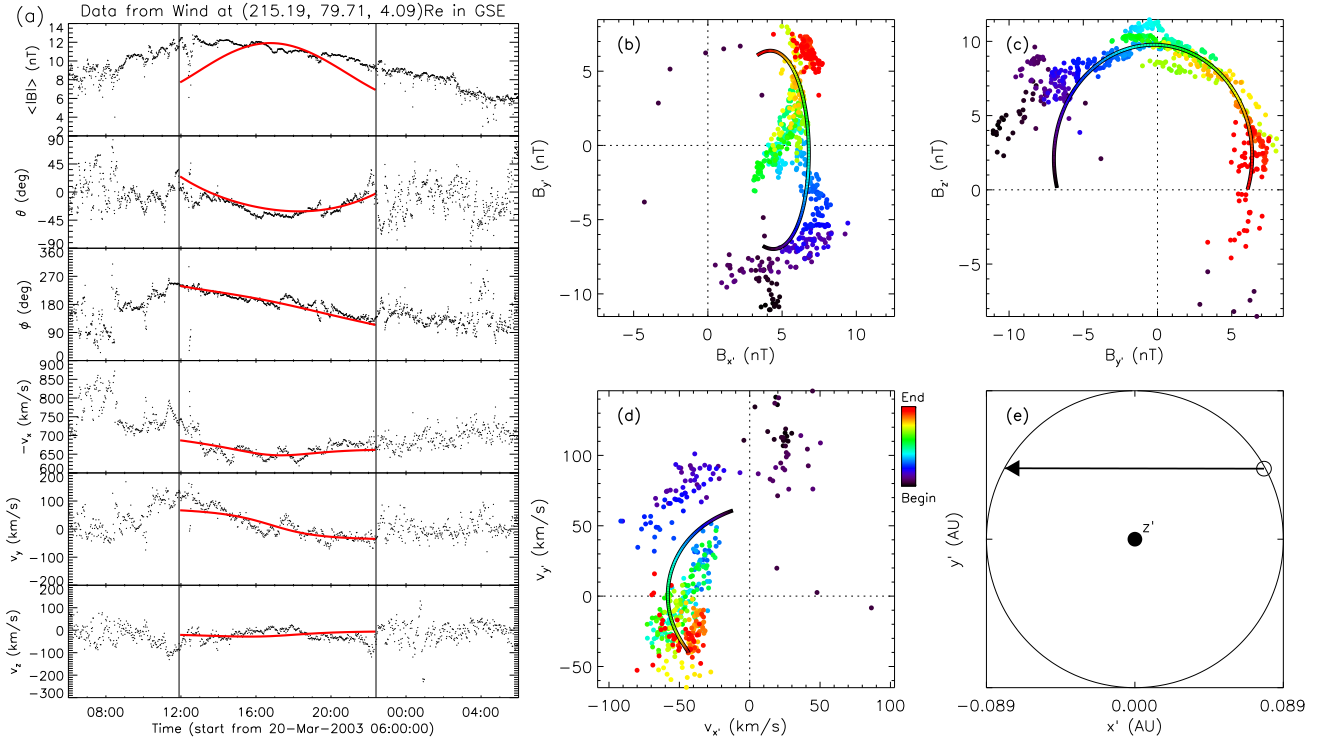


Figure 13: Similar to Fig. 12 but for an MC observed on March 20, 2003.

The second possible cause is that the angular momentum is generated internally all the time of the CME from its early phase in the corona to propagation phase in interplanetary space. It is well known that the magnetic energy of a CME will decrease when it expands [e.g., *Kumar and Rust, 1996; Wang et al., 2009; Nakwacki et al., 2011*]. The decreased magnetic energy may go into thermal energy and kinetic energy through some mechanisms. It means that the poloidal motion could be somehow generated inside the MC. If this is true, the decreased magnetic energy must partially go into the rotational kinetic energy, and we would expect that the poloidal speed, v_p , be more or less dependent on the radial propagation speed, v_X , because generally the faster the propagation speed is the larger is the rate of the magnetic energy decrease. As we can see in Figure 16b, there is also a weak correlation with a coefficient of 0.4. It suggests that the internal process perhaps is another factor for the poloidal motion. The numerical simulations of the evolution of magnetic flux rope by *Wei et al. [1991]* had shown that the expansion of a flux rope may cause the significantly azimuthal velocity, i.e., the poloidal speed in our study, even if the azimuthal velocity was zero initially.

The third one may be that the angular momentum is generated initially at the eruption of the CME in the corona, and carried all the way to 1 AU. The kinking/un-kinking behavior and rotation of the whole erupting magnetic structure are often observed in coronagraphs [e.g., *Yurchyshyn, 2008; Yurchyshyn et al., 2009; Vourlidas et al., 2011*]. Such processes might introduce poloidal motion in the body of the CME. However, if the angular momentum is conserved as that we treated in the model (see Eq.7), we may estimate that the poloidal speed will be about 200 times of that at 1 AU, or about 2000 km s⁻¹ near the Sun if the poloidal speed

is about 10 km s⁻¹ at 1 AU. It is interesting to check the imaging data of CMEs to search such a fast poloidal motion though no such a phenomenon was reported so far.

No matter which of the above speculation(s) is right, the evidence of poloidal motion inside MCs does shed a new light on the dynamic evolution of CMEs from its birth to interplanetary space. Some outstanding questions are open. How is the angular momentum in the solar wind transferred into an MC if the first speculation is right? How is the magnetic energy of an MC converted into the rotational kinetic energy if the second speculation is right? How does the poloidal motion depend on the heliocentric distance? Whether or how does the poloidal motion modify the macro/microscopic properties of an MC? Except further studies based on the current observations, the upcoming missions, Solar Orbiter and Solar Probe+ will provide great opportunities to advance our understanding of these questions.

Acknowledgments. We acknowledge the use of the data from Wind spacecraft. The model developed in this work could be run and tested online at http://space.ustc.edu.cn/dreams/mc_fitting/. We thank Dr. L. C. Lee for valuable discussion on the poloidal motion, and we are also grateful to the referees for constructive comments. This work is supported by the grants from MOST 973 key project (2011CB811403), CAS (Key Research Program KZZD-EW-01-4), NSFC (41131065 and 41121003), MOEC (20113402110001) and the fundamental research funds for the central universities.

A Derivation of poloidal speed v_φ

Under the self-similar assumption, we may assume the self-similarity variable $x = r/R(t)$, and the self-similarity solution $\rho(t, r) = \rho_0(t)f_\rho(x)$ and $v_\varphi(t, r) = v_0(t)f_p(x)$, which

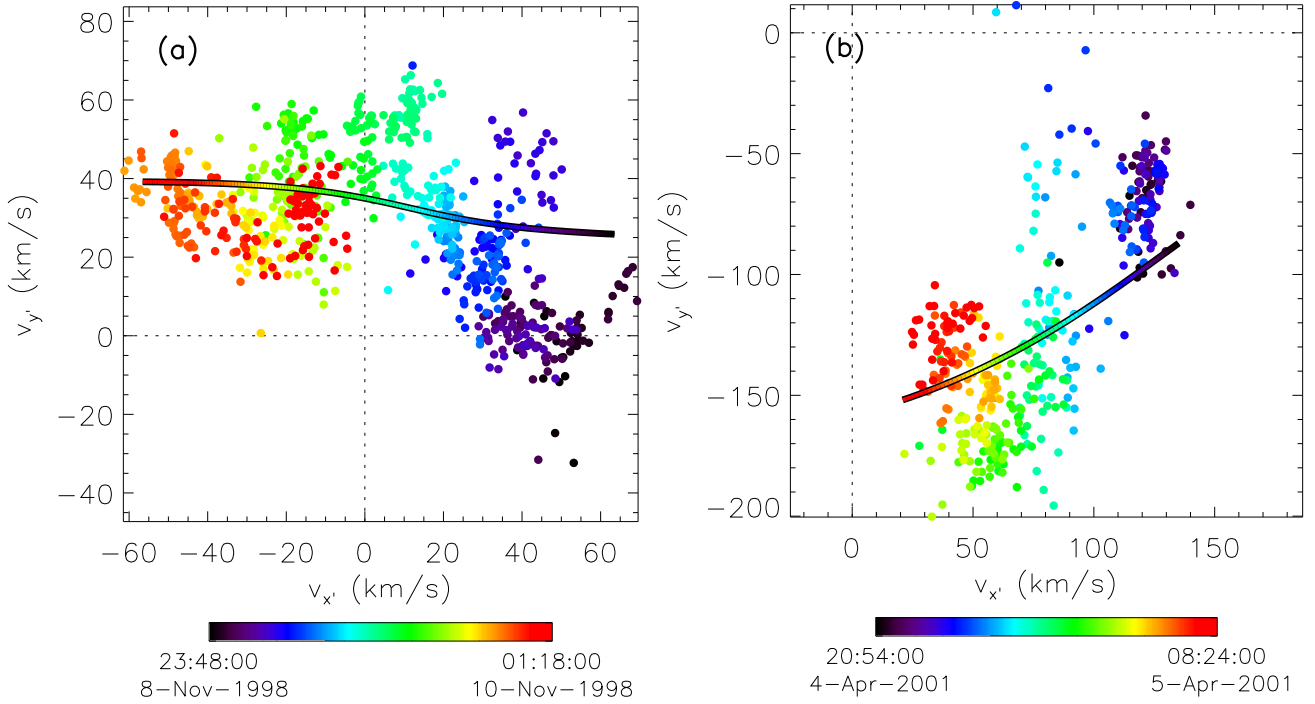


Figure 14: The scatter plots of the velocity components in the (x', y') plane for (a) the MC observed during November 8–10, 1998 and (b) the MC during April 4–5, 2001. The arrangement is as the same as that in Fig. 12d.

mean that the shape of the spatial distribution of ρ and v_φ along the radial distance in the flux rope will not change with time. Further we have the self-similarity solution of $v_r(t, r) = v_e(t)x = \frac{v_e(t)}{R(t)}r$, in which $v_e(t) = \frac{\partial R}{\partial t}$ is the expansion speed and $R(t)$ is the radius of the flux rope.

The mass conservation requires

$$\begin{aligned} \int \rho r dr d\varphi dz &= 2\pi l \int_0^R \rho r dr = 2\pi l R^2 \int_0^1 \rho x dx \\ &= 2\pi l R^2 \rho_0(t) \int_0^1 f_\rho(x) x dx = M \end{aligned} \quad (18)$$

where M is the total mass of the flux rope, and the above integral is a constant, say c_1 . Then we have

$$\rho_0(t) = \frac{M}{2\pi c_1} R^{-2} l^{-1} \quad (19)$$

The conservation of fluxes implies that $l \propto R$ (Eq.14) or $l = c_2 R$, and therefore the above equation becomes

$$\rho_0(t) = \frac{M}{2\pi c_1 c_2} R^{-3} \quad (20)$$

Similarly, if there is no force in $\hat{\varphi}$ direction, the conservation of angular momentum requires

$$\begin{aligned} \int \rho r v_\varphi r dr d\varphi dz &= 2\pi l R^3 \int_0^1 \rho v_\varphi x^2 dx \\ &= 2\pi l R^3 \rho_0(t) v_0(t) \int_0^1 f_\rho(x) f_p(x) x^2 dx = L_A \end{aligned} \quad (21)$$

where L_A is the total angular momentum, and the integral in the above equation is also a constant, say c_3 . Then we get

$$v_0(t) = \frac{L_A}{2\pi c_3} \rho_0^{-1} R^{-3} l^{-1} = \frac{c_1 L_A}{c_3 M} R^{-1} \quad (22)$$

or

$$v_0(t) = k_1 R^{-1} \quad (23)$$

where $k_1 = \frac{c_1 L_A}{c_3 M}$ is also a constant, and therefore expression of v_φ writes $k_1 f_p(x) R^{-1}$, as written in Eq.7.

B Additional tables

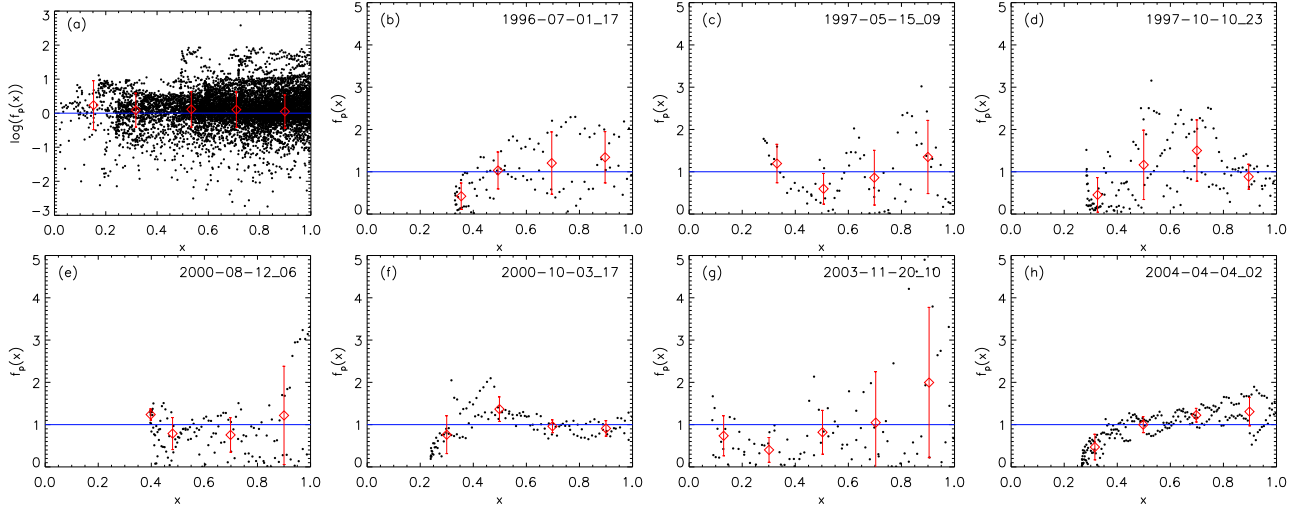


Figure 15: Scatter plot of measurements during the MC events showing the validity of the assumption of $f_p(x) = 1$ in Eq.7. Panel (a) contains all the data points of the 72 MC events, and each of the other panels display the data points in a selected MC. See the main text for more details.

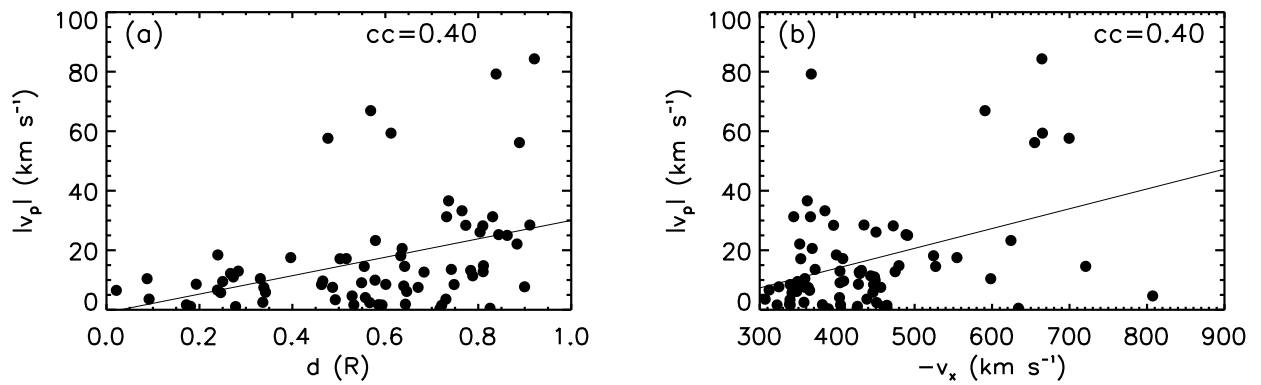


Figure 16: (a) Scatter plot showing the correlation between the poloidal speed and the closest approach and (b) that between the poloidal speed and radial propagation speed. The lines give the linear fitting results.

Table 2: Parameters of 72 MCs derived by the velocity-modified cylindrical force-free flux rope model

No. (1)	MC Interval		Modeled Parameters																	
	t_0 (2)	Δt (3)	B_0 (4)	R (5)	H (6)	θ (7)	ϕ (8)	d (9)	v_X (10)	v_Y (11)	v_Z (12)	v_e (13)	v_p (14)	Δt_c (15)	Θ (16)	Φ_z (17)	Φ_φ (18)	H_m (19)	E_{m0} (20)	χ_n (21)
1	1995/02/08 05:48	19.0	15	0.09	-1	-10	122	-0.56	-403	2	14	30	4	8.8	57	0.40	3.41±0.76	-1.72±0.38	2.52±0.56	0.26
2	1995/04/03 07:48	27.0	14	0.22	1	5	75	-0.84	-366	0	68	31	-79	12.8	75	2.0	7.3±1.6	18.4±4.1	11.7±2.6	0.27
3	1995/04/06 07:18	10.5	11	0.06	-1	45	119	-0.74	-361	-9	-9	-17	-36	5.5	69	0.14	1.75±0.39	-0.309±0.069	0.66±0.15	0.36
4	1995/08/22 21:18	22.0	13	0.10	1	-26	308	-0.64	-352	10	-20	20	7	10.4	55	0.41	3.22±0.72	1.65±0.37	2.25±0.50	0.28
5	1995/10/18 19:48	29.5	24	0.10	1	0	314	-0.17	-404	-5	13	-23	-1	15.9	45	0.8	6.0±1.3	6.0±1.3	7.8±1.7	0.29
6	1996/05/27 15:18	40.0	10	0.16	-1	5	119	-0.02	-364	-20	-5	12	-6	19.3	60	0.79	3.93±0.87	-3.85±0.86	3.35±0.74	0.33
7	1996/07/01 17:18	17.0	12	0.07	-1	4	75	0.33	-358	-20	-9	14	10	8.1	75	0.21	2.19±0.49	-0.56±0.12	1.04±0.23	0.40
8	1996/08/07 12:18	22.5	9	0.11	1	-39	236	0.65	-347	0	14	7	6	11.1	64	0.33	2.32±0.52	0.97±0.21	1.17±0.26	0.36
9	1996/12/24 02:48	32.5	14	0.16	1	29	60	-0.60	-350	-15	26	25	-8	15.1	64	1.0	5.2±1.1	6.5±1.4	5.8±1.3	0.29
10	1997/01/10 05:18	21.0	17	0.10	1	-29	240	-0.09	-438	11	-16	42	3	9.4	64	0.49	3.92±0.87	2.41±0.54	3.33±0.74	0.26
11	1997/04/11 05:36	13.5	26	0.02	1	14	1	-0.80	-450	-17	-34	12	26	6.2	14	0.04	1.37±0.30	0.064±0.014	0.405±0.090	0.45
12	1997/05/15 09:06	16.0	21	0.09	-1	-15	104	0.27	-448	37	0	-14	-11	8.3	75	0.46	4.23±0.95	-2.41±0.54	3.88±0.86	0.37
13	1997/06/09 02:18	21.0	17	0.04	1	-4	195	0.74	-371	1	6	3	13	10.3	15	0.08	1.58±0.35	0.157±0.035	0.54±0.12	0.35
14	1997/09/22 00:48	16.5	23	0.10	-1	51	33	0.68	-428	45	3	62	12	7.3	58	0.71	5.54±1.23	-4.9±1.1	6.7±1.5	0.17
15	1997/10/01 16:18	30.5	15	0.03	-1	6	178	-0.79	-443	0	3	-7	11	16.6	7	0.04	1.07±0.24	-0.054±0.012	0.248±0.055	0.28
16	1997/10/10 23:48	25.0	14	0.11	1	-8	240	-0.28	-403	13	-11	37	-12	11.3	60	0.52	3.67±0.81	2.37±0.53	2.92±0.65	0.27
17	1997/11/07 15:48	12.5	26	0.08	1	27	313	-0.78	-431	0	9	20	-13	6.0	52	0.5	5.1±1.1	3.48±0.77	5.7±1.3	0.16
18	1997/11/08 04:54	10.0	20	0.05	1	52	5	-0.64	-367	-2	3	18	20	4.7	52	0.13	2.21±0.49	0.353±0.078	1.06±0.24	0.27
19	1998/01/07 03:18	29.0	22	0.16	-1	60	134	-0.59	-380	-26	-1	31	-1	13.4	69	1.6	8.2±1.8	-16.4±3.6	14.5±3.2	0.26
20	1998/02/04 04:30	42.0	14	0.11	-1	4	32	-0.59	-322	10	14	34	-1	17.8	32	0.55	3.86±0.86	-2.67±0.59	3.24±0.72	0.27
21	1998/03/04 14:18	40.0	14	0.17	-1	16	60	0.53	-339	-2	-12	20	-1	18.8	61	1.2	5.5±1.2	-8.1±1.8	6.7±1.5	0.28
22	1998/06/02 10:36	5.3	15	0.02	-1	14	34	0.52	-407	-21	-46	15	17	2.5	37	0.01	0.58±0.13	-0.009±0.002	0.072±0.016	0.20
23	1998/06/24 16:48	29.0	16	0.03	-1	10	174	-0.46	-447	-8	17	1	8	14.3	11	0.05	1.24±0.28	-0.080±0.018	0.336±0.075	0.28
24	1998/08/20 10:18	33.0	15	0.11	1	1	299	-0.24	-312	-5	-17	25	6	14.9	60	0.56	3.99±0.89	2.80±0.62	3.46±0.77	0.36
25	1998/09/25 10:18	27.0	17	0.21	-1	60	195	0.58	-624	94	50	90	-23	11.6	61	2.33	8.72±1.94	-25.4±5.6	16.5±3.7	0.23
26	1998/11/08 23:48	25.5	19	0.15	1	-60	134	0.49	-456	-33	10	68	-7	10.9	69	1.3	6.8±1.5	11.0±2.4	10.0±2.2	0.31
27	1999/08/09 10:48	29.0	12	0.04	-1	15	176	-0.49	-339	5	-18	-10	-3	15.8	15	0.07	1.28±0.28	-0.112±0.025	0.355±0.079	0.30
28	2000/07/01 08:48	18.5	12	0.11	-1	60	178	-0.77	-384	23	9	-14	33	9.4	60	0.48	3.32±0.74	-1.99±0.44	2.39±0.53	0.25
29	2000/07/28 21:06	13.0	21	0.11	-1	-11	240	-0.81	-474	-14	1	4	-12	6.5	60	0.7	5.4±1.2	-5.0±1.1	6.2±1.4	0.29
30	2000/08/12 06:06	23.0	29	0.14	-1	9	60	0.40	-554	-1	-35	63	-17	10.2	60	1.8	9.9±2.2	-22.0±4.9	21.1±4.7	0.42

Table 3: Parameters of 72 MCs derived by the velocity-modified cylindrical force-free flux rope model (continued)

No. (1)	MC Interval		Modeled Parameters																	
	t_0 (2)	Δt (3)	B_0 (4)	R (5)	H (6)	θ (7)	ϕ (8)	d (9)	v_X (10)	v_Y (11)	v_Z (12)	v_e (13)	v_p (14)	Δt_c (15)	Θ (16)	Φ_z (17)	Φ_φ (18)	H_m (19)	E_{m0} (20)	χ_n (21)
31	2000/10/03 17:06	21.0	19	0.09	1	33	59	0.24	-398	7	-13	16	-18	10.0	65	0.50	4.17±0.93	2.59±0.57	3.78±0.84	0.24
32	2000/10/13 18:24	22.5	18	0.02	-1	6	188	0.77	-395	-22	10	0	-28	11.3	10	0.03	0.94±0.21	-0.030±0.007	0.190±0.042	0.21
33	2000/11/06 23:06	19.0	28	0.08	-1	0	150	-0.55	-527	-17	-32	-13	-14	9.8	29	0.5	5.2±1.1	-3.21±0.71	5.8±1.3	0.21
34	2001/03/19 23:18	19.0	25	0.02	-1	-11	185	-0.55	-403	-13	-25	-9	9	10.6	12	0.02	0.99±0.22	-0.025±0.006	0.213±0.047	0.20
35	2001/04/04 20:54	11.5	17	0.23	-1	18	272	-0.92	-664	-39	-80	132	84	5.3	87	2.8	9.5±2.1	-33.0±7.3	19.5±4.3	0.29
36	2001/04/12 07:54	10.0	26	0.07	1	6	196	0.89	-654	83	-63	97	56	4.2	17	0.41	4.47±0.99	2.29±0.51	4.34±0.96	0.31
37	2001/04/22 00:54	24.5	15	0.10	-1	-45	309	0.34	-357	0	4	33	-2	11.0	63	0.45	3.62±0.80	-2.05±0.45	2.84±0.63	0.18
38	2001/04/29 01:54	11.0	16	0.13	-1	19	60	0.83	-634	15	-39	39	0	5.3	62	0.8	4.9±1.1	-4.9±1.1	5.2±1.1	0.19
39	2001/05/28 11:54	22.5	13	0.07	-1	-14	25	0.57	-450	26	42	-1	2	11.3	29	0.21	2.27±0.50	-0.61±0.14	1.12±0.25	0.22
40	2001/07/10 17:18	39.5	8	0.13	1	15	224	-0.25	-348	-4	-12	2	-9	19.6	46	0.37	2.35±0.52	1.09±0.24	1.19±0.27	0.41
41	2002/03/19 22:54	16.5	24	0.09	1	11	136	0.83	-343	-3	4	-12	-31	8.5	44	0.5	4.9±1.1	3.33±0.74	5.3±1.2	0.20
42	2002/03/24 03:48	43.0	16	0.18	1	29	314	-0.19	-427	-1	-7	-1	8	21.6	52	1.5	6.7±1.5	12.6±2.8	9.7±2.2	0.39
43	2002/04/18 04:18	22.0	20	0.06	1	-6	346	-0.81	-479	-2	-5	7	-14	10.6	15	0.21	2.83±0.63	0.75±0.17	1.74±0.39	0.17
44	2002/05/19 03:54	19.5	18	0.25	-1	-15	87	0.91	-434	2	-59	78	-28	9.0	87	3.3	10.6±2.3	-43.4±9.6	24.3±5.4	0.29
45	2002/08/02 07:24	13.7	20	0.10	-1	-8	311	0.81	-472	1	14	25	-28	6.5	49	0.6	4.7±1.0	-3.48±0.77	4.8±1.1	0.14
46	2002/09/03 00:18	18.5	13	0.06	1	29	196	0.50	-352	-3	-32	-21	17	10.1	33	0.13	1.77±0.39	0.276±0.061	0.68±0.15	0.44
47	2003/03/20 11:54	10.5	14	0.09	-1	-60	208	0.48	-699	10	0	18	57	5.1	64	0.35	3.03±0.67	-1.32±0.29	1.99±0.44	0.34
48	2003/08/18 11:36	16.8	24	0.10	1	-23	191	0.86	-490	-11	50	21	25	8.0	26	0.7	5.7±1.3	5.3±1.2	7.1±1.6	0.30
49	2003/11/20 10:48	15.5	33	0.10	1	-60	134	0.09	-598	-6	27	106	10	6.3	69	1.1	8.2±1.8	11.1±2.4	14.7±3.3	0.38
50	2004/04/04 02:48	36.0	18	0.17	-1	60	25	-0.27	-429	15	-7	25	-12	16.8	63	1.6	7.3±1.6	-14.4±3.2	11.5±2.6	0.33
51	2004/07/24 12:48	24.5	27	0.19	1	-36	45	-0.57	-590	72	9	11	-66	11.9	55	2.8	12.1±2.7	42.9±9.5	31.8±7.1	0.26
52	2004/08/29 18:42	26.1	18	0.16	1	-16	119	0.72	-388	-7	-1	16	0	12.6	61	1.3	6.5±1.4	10.3±2.3	9.1±2.0	0.33
53	2004/11/08 03:24	13.2	24	0.03	-1	-2	8	0.61	-664	62	-27	42	59	5.3	8	0.07	1.81±0.40	-0.167±0.037	0.71±0.16	0.49
54	2004/11/09 20:54	6.5	46	0.06	-1	23	311	0.53	-807	10	15	37	4	3.0	53	0.49	6.55±1.46	-4.02±0.89	9.3±2.1	0.31
55	2004/11/10 03:36	7.5	35	0.06	-1	-41	10	0.64	-720	-50	-10	66	-14	3.3	42	0.3	4.8±1.1	-2.07±0.46	5.0±1.1	0.16
56	2005/05/20 07:18	22.0	12	0.12	-1	60	225	-0.34	-446	0	-2	7	5	10.8	69	0.51	3.43±0.76	-2.20±0.49	2.55±0.57	0.47
57	2005/06/12 15:36	15.5	26	0.06	-1	-17	4	0.84	-488	28	-28	31	25	7.0	18	0.31	3.87±0.86	-1.51±0.33	3.26±0.72	0.22
58	2005/07/17 15:18	12.5	13	0.06	1	-29	60	0.18	-426	-8	-25	32	1	5.8	64	0.14	1.89±0.42	0.333±0.074	0.77±0.17	0.30
59	2005/12/31 14:48	20.0	13	0.02	1	0	353	-0.72	-464	-2	17	-11	1	11.5	6	0.02	0.60±0.13	0.011±0.002	0.077±0.017	0.22
60	2006/02/05 19:06	18.0	11	0.07	1	-30	119	0.25	-341	-12	-5	24	5	8.3	64	0.16	1.81±0.40	0.36±0.08	0.71±0.16	0.38

Table 4: Parameters of 72 MCs derived by the velocity-modified cylindrical force-free flux rope model (continued)

No. (1)	MC Interval		Modeled Parameters																	
	t_0 (2)	Δt (3)	B_0 (4)	R (5)	H (6)	θ (7)	ϕ (8)	d (9)	v_X (10)	v_Y (11)	v_Z (12)	v_e (13)	v_p (14)	Δt_c (15)	Θ (16)	Φ_z (17)	Φ_φ (18)	H_m (19)	E_{m0} (20)	χ_n (21)
61	2006/04/13 20:36	13.3	25	0.08	-1	-5	226	-0.63	-524	22	6	-2	-18	6.7	46	0.5	4.9±1.1	-3.11±0.69	5.2±1.2	0.23
62	2006/08/30 21:06	17.8	10	0.07	-1	-5	224	-0.47	-408	0	3	8	-9	8.7	44	0.15	1.66±0.37	-0.302±0.067	0.60±0.13	0.26
63	2007/05/21 22:54	14.7	14	0.02	-1	-11	350	-0.58	-449	20	26	-14	9	8.5	14	0.01	0.58±0.13	-0.009±0.002	0.072±0.016	0.39
64	2007/11/19 23:24	13.5	18	0.06	-1	-10	314	0.28	-460	-15	23	18	-1	6.3	46	0.18	2.52±0.56	-0.58±0.13	1.38±0.31	0.49
65	2008/12/17 03:06	11.3	12	0.03	-1	0	209	-0.64	-338	0	9	17	1	5.2	29	0.03	0.86±0.19	-0.034±0.008	0.161±0.036	0.22
66	2009/02/04 00:06	10.8	14	0.04	1	2	146	0.67	-358	-7	-12	11	-7	5.2	33	0.06	1.22±0.27	0.085±0.019	0.322±0.071	0.33
67	2009/03/12 00:42	24.0	12	0.10	1	42	122	0.34	-362	-13	0	-26	7	12.9	67	0.39	2.97±0.66	1.44±0.32	1.92±0.43	0.43
68	2009/07/21 03:54	13.2	13	0.05	1	2	155	0.90	-324	-1	-4	-2	7	6.7	24	0.10	1.58±0.35	0.198±0.044	0.54±0.12	0.21
69	2009/09/10 10:24	6.0	8	0.02	1	20	150	0.73	-306	2	0	3	3	3.0	35	0.008	0.356±0.079	0.004±0.001	0.027±0.006	0.22
70	2009/09/30 07:54	9.0	13	0.04	-1	28	219	-0.75	-339	1	16	1	8	4.5	47	0.06	1.23±0.27	-0.095±0.021	0.326±0.072	0.25
71	2009/10/12 12:06	4.8	10	0.004	-1	4	351	0.73	-365	10	-8	0	-31	2.5	9	0.001	0.097±0.022	-6e-5±1e-5	20e-4±5e-4	0.18
72	2009/11/01 08:48	23.0	8	0.11	-1	10	205	-0.88	-351	10	-14	2	-22	11.4	27	0.28	2.11±0.47	-0.73±0.16	0.96±0.21	0.39

Note 1: Column 2 is the begin time of an MC in UT. Column 3 is the duration of the observed MC interval in units of hour. The interpretations of all the other columns could be found in Table 1 with the difference that Column 15 is $\Delta t_c = t_c - t_0$. The values of B_0 , R and v_p are all obtained at the time of t_c . One can refer to Sec.2.1 for more details.

Note 2: For the modeled parameters, B_0 is in units of nT, R in units of AU, θ , ϕ and Θ in units of degree, d in units of R , all the speeds are in units of km s⁻¹, Δt_c in units of hour, Φ_z and Φ_φ in units of 10²¹ Mx, H_m in units of 10⁴² Mx², and E_{m0} in units of 10³¹ erg.

References

- Al-Haddad, N., I. I. Roussev, C. Möstl, C. Jacobs, N. Lugaz, S. Poedts, and C. J. Farrugia, On the internal structure of the magnetic field in magnetic clouds and interplanetary coronal mass ejections: Writhe versus twist, *Astrophys. J. Lett.*, *738*, L18(6pp), 2011.
- Al-Haddad, N., T. Nieves-Chinchilla, N. P. Savani, C. Möstl, K. Marubashi, M. A. Hidalgo, I. I. Roussev, S. Poedts, and C. J. Farrugia, Magnetic field configuration models and reconstruction methods for interplanetary coronal mass ejections, *Sol. Phys.*, *284*, 129–149, 2013.
- Berdichevsky, D. B., R. P. Lepping, and C. J. Farrugia, Geometric considerations of the evolution of magnetic flux ropes, *Phys. Rev. E*, *67*, 036405, 2003.
- Berger, M. A., Topological quantities in magnetohydrodynamics, in *Advances in Nonlinear Dynamics*, edited by A. Ferriz-Mas and M. Núñez, p. 345, London: Taylor and Francis Group, 2003.
- Bothmer, V., and R. Schwenn, The structure and origin of magnetic clouds in the solar wind, *Ann. Geophys.*, *16*, 1, 1998.
- Burlaga, L., E. Sittler, F. Mariani, and R. Schwenn, Magnetic loop behind an interplanetary shock: Voyager, Helios, and IMP 8 observations, *J. Geophys. Res.*, *86*, 6673–6684, 1981.
- Burlaga, L. F., Magnetic clouds and force-free field with constant alpha, *J. Geophys. Res.*, *93*, 7217, 1988.
- Cid, C., M. A. Hidalgo, T. Nieves-Chinchilla, J. Sequeiros, and A. F. Viñas, Plasma and magnetic field inside magnetic clouds: a global study, *Sol. Phys.*, *207*, 187–198, 2002.
- Dasso, S., C. H. Mandrini, P. Démoulin, M. L. Luoni, and A. M. Gulisano, Large scale mhd properties of interplanetary magnetic clouds, *Adv. in Space Res.*, *35*, 711–724, 2005.
- Dasso, S., M. S. Nakwacki, P. Démoulin, and C. H. Mandrini, Progressive transformation of a flux rope to an ICME. comparative analysis using the direct and fitted expansion methods, *Sol. Phys.*, *244*, 115–137, 2007.
- Dasso, S., C. H. Mandrini, B. Schmieder, H. Cremades, C. Cid, Y. Cerrato, E. Saiz, P. Démoulin, A. N. Zhukov, L. Rodriguez, A. Aran, M. Menvielle, and S. Poedts, Linking two consecutive nonmerging magnetic clouds with their solar sources, *J. Geophys. Res.*, *114*, A02109, 2009.
- Démoulin, P., and S. Dasso, Causes and consequences of magnetic cloud expansion, *Astron. & Astrophys.*, *498*, 551–566, 2009a.
- Démoulin, P., and S. Dasso, Magnetic cloud models with bent and oblate cross-section boundaries, *Astron. & Astrophys.*, *507*, 969–980, 2009b.
- Démoulin, P., M. S. Nakwacki, S. Dasso, and C. H. Mandrini, Expected in situ velocities from a hierarchical model for expanding interplanetary coronal mass ejections, *Sol. Phys.*, *250*, 347–374, 2008.
- Démoulin, P., S. Dasso, and M. Janvier, Does spacecraft trajectory strongly affect detection of magnetic clouds?, *Astron. & Astrophys.*, *550*, A3, 2013.
- Farrugia, C. J., L. F. Burlaga, V. A. Osherovich, I. G. Richardson, M. P. Freeman, R. P. Lepping, and A. J. Lazarus, A study of an expanding interplanetary magnetic cloud and its interaction with the earth’s magnetosphere – the interplanetary aspect, *J. Geophys. Res.*, *98(A5)*, 7621–7632, 1993.
- Farrugia, C. J., V. A. Osherovich, and L. F. Burlaga, Magnetic flux rope versus the spheromak as models for interplanetary magnetic clouds, *J. Geophys. Res.*, *100*, 12,293, 1995.
- Goldstein, H., On the field configuration in magnetic clouds, in *Sol. Wind Five*, p. 731, NASA Conf. Publ. 2280, Washington D. C., 1983.
- Gulisano, A. M., P. Démoulin, S. Dasso, M. E. Ruiz, and E. Marsch, Global and local expansion of magnetic clouds in the inner heliosphere, *Astron. & Astrophys.*, *509*, A39, 2010.
- Gulisano, A. M., P. Démoulin, S. Dasso, and L. Rodriguez, Expansion of magnetic clouds in the outer heliosphere, *Astron. & Astrophys.*, *543*, A107, 2012.
- Hidalgo, M. A., A study of the expansion and distortion of the cross section of magnetic clouds in the interplanetary medium, *J. Geophys. Res.*, *108*, 1320, 2003.
- Hidalgo, M. A., and T. Nieves-Chinchilla, A global magnetic topology model for magnetic clouds. i., *Astrophys. J.*, *748*, 109(7pp), 2012.
- Hidalgo, M. A., C. Cid, A. F. Vinas, and J. Sequeiros, A non-force-free approach to the topology of magnetic clouds in the solar wind, *J. Geophys. Res.*, *107*, 1002, 2002a.
- Hidalgo, M. A., T. Nieves-Chinchilla, and C. Cid, Elliptical cross-section model for the magnetic topology of magnetic clouds, *Geophys. Res. Lett.*, *29*, 1637, 2002b.
- Hu, Q., and B. U. Ö. Sonnerup, Reconstruction of magnetic flux ropes in the solar wind, *Geophys. Res. Lett.*, *28*, 467–470, 2001.
- Hu, Q., and B. U. O. Sonnerup, Reconstruction of magnetic clouds in the solar wind: Orientations and configurations, *J. Geophys. Res.*, *107*, 1142, 2002.
- Isavnin, A., A. Vourlidas, and E. K. J. Kilpua, Three-dimensional evolution of erupted flux ropes from the Sun (2–20 r_☉) to 1 AU, *Sol. Phys.*, *284*, 203–215, 2013.
- Isavnin, A., A. Vourlidas, and E. K. J. Kilpua, Three-dimensional evolution of flux-rope CMEs and its relation to the local orientation of the heliospheric current sheet, *Sol. Phys.*, *289*, 2141–2156, 2014.

- Janvier, M., P. Démoulin, and S. Dasso, Global axis shape of magnetic clouds deduced from the distribution of their local axis orientation, *Astron. & Astrophys.*, 556, A50, 2013.
- Jian, L., C. T. Russell, J. G. Luhmann, and R. M. Skoug, Properties of interplanetary coronal mass ejections at one au during 1995 – 2004, *Sol. Phys.*, 239, 393–436, 2006.
- Kilpua, E. K. J., J. Pomoell, A. Vourlidas, R. Vainio, J. Luhmann, Y. Li, P. Schroeder, A. B. Galvin, and K. Simunac, STEREO observations of interplanetary coronal mass ejections and prominence deflection during solar minimum period, *Ann. Geophys.*, 27, 4491–4503, 2009.
- Klein, L. W., and L. F. Burlaga, Interplanetary magnetic clouds at 1 AU, *J. Geophys. Res.*, 87, 613–624, 1982.
- Kumar, A., and D. M. Rust, Interplanetary magnetic clouds, helicity conservation, and current-core flux-ropes, *J. Geophys. Res.*, 101, 15,667–15,684, 1996.
- Larson, D. E., R. P. Lin, J. M. McTiernan, J. P. McFadden, R. E. Ergun, M. McCarthy, H. Rème, T. R. Sanderson, M. Kaiser, R. P. Lepping, and J. Mazur, Tracing the topology of the october 18-20, 1995, magnetic cloud with $\sim 0.1 - 10^2$ keV electrons, *Geophys. Res. Lett.*, 24(15), 1911–1914, 1997.
- Lepping, R. P., J. A. Jones, and L. F. Burlaga, Magnetic field structure of interplanetary magnetic clouds at 1 AU, *J. Geophys. Res.*, 95, 11,957–11,965, 1990.
- Lepping, R. P., D. B. Berdichevsky, C.-C. Wu, A. Szabo, T. Narock, F. Mariani, A. J. Lazarus, and A. J. Quivers, A summary of WIND magnetic clouds for years 1995–2003: model-fitted parameters, associated errors and classifications, *Ann. Geophys.*, 24, 215–245, 2006.
- Lugaz, N., Accuracy and limitations of fitting and stereoscopic methods to determine the direction of coronal mass ejections from heliospheric imagers observations, *Sol. Phys.*, 267, 411–429, 2010.
- Lugaz, N., C. J. Farrugia, W. B. Manchester, IV, and N. Schwadron, The interaction of two coronal mass ejections: Influence of relative orientation, *Astrophys. J.*, 778, 20(14pp), 2013.
- Lundquist, S., Magnetohydrostatic fields, *Ark. Fys.*, 2, 361, 1950.
- Markwardt, C. B., Non-linear least squares fitting in IDL with MPFIT, in *Astronomical Data Analysis Software and Systems XVIII, ASP Conference Series*, vol. 411, edited by D. Bohlender, P. Dowler, and D. Durand, pp. 251–254, 2009.
- Marubashi, K., Structure of the interplanetary magnetic clouds and their solar origins, *Adv. in Space Res.*, 6, 335–338, 1986.
- Marubashi, K., Interplanetary magnetic flux ropes and solar filaments, in *Coronal Mass Ejections*, edited by N. Crooker, J. A. Joselyn, and J. Feynman, Geophys. Monogr. Ser. 99, pp. 147–156, AGU, 1997.
- Marubashi, K., and R. P. Lepping, Long-duration magnetic clouds: a comparison of analyses using torus- and cylinder-shaped flux rope models, *Ann. Geophys.*, 25, 2453–2477, 2007.
- Marubashi, K., K.-S. Cho, Y.-H. Kim, Y.-D. Park, and S.-H. Park, Geometry of the 20 November 2003 magnetic cloud, *J. Geophys. Res.*, 117, A01,101, 2012.
- More, J., The Levenberg-Marquardt algorithm: Implementation and theory, in *Numerical Analysis*, vol. 630, edited by G. A. Watson, p. 105, 1978.
- Mulligan, T., and C. T. Russell, Multispacecraft modeling of the flux rope structure of interplanetary coronal mass ejections: Cylindrically symmetric versus nonsymmetric topologies, *J. Geophys. Res.*, 106(A6), 10,581–10,596, 2001.
- Nakwacki, M. S., S. Dasso, C. H. Mandrini, and P. Démoulin, Analysis of large scale MHD quantities in expanding magnetic clouds, *J. Atmos. Solar-Terres. Phys.*, 70, 1318–1326, 2008.
- Nakwacki, M. S., S. Dasso, P. Démoulin, C. H. Mandrini, and A. M. Gulisano, Dynamical evolution of a magnetic cloud from the sun to 5.4 AU, *Astron. & Astrophys.*, 535, A52, 2011.
- Nieves-Chinchilla, T., R. Colaninno, A. Vourlidas, A. Szabo, R. P. Lepping, S. A. Boardsen, B. J. Anderson, and H. Korth, Remote and in situ observations of an unusual earth-directed coronal mass ejection from multiple viewpoints, *J. Geophys. Res.*, 117, A06,106, 2012.
- Owens, M. J., V. G. Merkin, and P. Riley, A kinematically distorted flux rope model for magnetic clouds, *J. Geophys. Res.*, 111, A03,104, 2006.
- Qiu, J., Q. Hu, T. A. Howard, and V. B. Yurchyshyn, On the magnetic flux budget in low-corona magnetic reconnection and interplanetary coronal mass ejections, *Astrophys. J.*, 659, 758–772, 2007.
- Riley, P., and N. U. Crooker, Kinematic treatment of coronal mass ejection evolution in the solar wind, *Astrophys. J.*, 600, 1035–1042, 2004.
- Riley, P., J. A. Linker, Z. Mikic, D. Odstrcil, T. H. Zurbuchen, and R. P. Lario, D. and Lepping, Using an MHD simulation to interpret the global context of a coronal mass ejection observed by two spacecraft, *J. Geophys. Res.*, 108, 1272, 2003.
- Riley, P., J. A. Linker, R. Lionello, Z. Mikić, D. Odstrcil, M. A. Hidalgo, C. Cid, Q. Hu, R. P. Lepping, B. J. Lynch, and A. Rees, Fitting flux ropes to a global MHD solution: a comparison of techniques, *J. Atmos. Solar-Terres. Phys.*, 66, 1321–1331, 2004.
- Rodriguez, L., M. Mierla, A. Zhukov, M. West, and E. Kilpua, Linking remote-sensing and in situ observations of coronal mass ejections using STEREO, *Sol. Phys.*, 270, 561–573, 2011.

- Romashets, E. P., and M. Vandas, Force-free field inside a toroidal magnetic cloud, *Geophys. Res. Lett.*, *30*, 2065, 2003.
- Rust, K., B. J. Anderson, M. D. Andrews, M. H. Acuna, C. T. Russell, P. W. Schuck, and T. Mulligan, Comparison of interplanetary disturbances at the NEAR spacecraft with coronal mass ejections at the SUN, *Astrophys. J.*, *621*, 524–536, 2005.
- Savani, N. P., A. P. Rouillard, J. A. Davies, M. J. Owens, R. J. Forsyth, C. J. Davis, and R. A. Harrison, The radial width of a coronal mass ejection between 0.1 and 0.4 AU estimated from the heliospheric imager on STEREO, *Ann. Geophys.*, *27*, 4349–4358, 2009.
- Schwenn, R., A. Dal Lago, E. Huttunen, and W. D. Gonzalez, The association of coronal mass ejections with their effects near the Earth, *Ann. Geophys.*, *23(3)*, 1033–1059, 2005.
- Shimazu, H., and M. Vandas, A self-similar solution of expanding cylindrical flux ropes for any polytropic index value, *Earth Planets Space*, *54*, 783–790, 2002.
- Vandas, M., and E. P. Romashets, A force-free field with constant alpha in an oblate cylinder: A generalization of the lundquist solution, *Astron. & Astrophys.*, *398*, 801–807, 2003.
- Vourlidas, A., R. A. Howard, E. Esfandiari, S. Patsourakos, S. Yashiro, and G. Michalek, Comprehensive analysis of coronal mass ejection mass and energy properties over a full solar cycle, *Astrophys. J.*, *722*, 1522–1538, 2010.
- Vourlidas, A., R. Colaninno, T. Nieves-Chinchilla, and G. Stenborg, The first observation of a rapidly rotating coronal mass ejection in the middle corona, *Astrophys. J. Lett.*, *733*, L23(6pp), 2011.
- Wang, C., D. Du, and J. D. Richardson, Characteristics of the interplanetary coronal mass ejections in the heliosphere between 0.3 and 5.4 AU, *J. Geophys. Res.*, *110*, A10,107, 2005.
- Wang, Y., P. Z. Ye, S. Wang, G. P. Zhou, and J. X. Wang, A statistical study on the geoeffectiveness of earth-directed coronal mass ejections from March 1997 to December 2000, *J. Geophys. Res.*, *107(A11)*, 1340, doi:10.1029/2002JA009,244, 2002.
- Wang, Y., C. Shen, P. Ye, and S. Wang, Deflection of coronal mass ejection in the interplanetary medium, *Sol. Phys.*, *222*, 329–343, 2004.
- Wang, Y., X. Xue, C. Shen, P. Ye, S. Wang, and J. Zhang, Impact of the major coronal mass ejections on geo-space during September 7 – 13, 2005, *Astrophys. J.*, *646*, 625–633, 2006a.
- Wang, Y., G. Zhou, P. Ye, S. Wang, and J. Wang, A study on the orientation of interplanetary magnetic clouds and solar filaments, *Astrophys. J.*, *651*, 1245–1255, 2006b.
- Wang, Y., J. Zhang, and C. Shen, An analytical model probing the internal state of coronal mass ejections based on observations of their expansions and propagations, *J. Geophys. Res.*, *114*, A10,104, 2009.
- Wang, Y., B. Wang, C. Shen, F. Shen, and N. Lugaz, Deflected propagation of a coronal mass ejection from the corona to interplanetary space, *J. Geophys. Res.*, *accepted*, 2014.
- Wei, C. Q., L. C. Lee, S. Wang, and S.-I. Akasofu, Evolution of magnetic flux ropes associated with flux transfer events and interplanetary magnetic clouds, *J. Geophys. Res.*, *96*, 1619–1632, 1991.
- Xiong, M., H. Zheng, Y. Wang, and S. Wang, Magnetohydrodynamic simulation of the interaction between interplanetary strong shock and magnetic cloud and its consequent geoeffectiveness: 2. oblique collision, *J. Geophys. Res.*, *111*, A11,102, 2006.
- Xiong, M., H. Zheng, S. T. Wu, Y. Wang, and S. Wang, Magnetohydrodynamic simulation of the interaction between two interplanetary magnetic clouds and its consequent geoeffectiveness, *J. Geophys. Res.*, *112*, A11,103, 2007.
- Yurchyshyn, V., Relationship between EIT posteruption arcades, coronal mass ejections, the coronal neutral line, and magnetic clouds, *Astrophys. J. Lett.*, *675*, L49–L52, 2008.
- Yurchyshyn, V., V. Abramenko, and D. Tripathi, Rotation of white-light coronal mass ejection structures as inferred from LASCO coronagraph, *Astrophys. J.*, *705*, 426–435, 2009.